Applying the Dark Target aerosol algorithm with Advanced Himawari Imager observations during the KORUS-AQ field campaign

Pawan Gupta[1, 2], Robert C. Levy[3], Shana Mattoo[3, 4], Lorraine A. Remer[5], Robert E. Holz[6], Andrew K. Heidinger[7]

[1] {STI, Universities Space Research Association (USRA), Huntsville, AL, USA}

[2] {NASA Marshall Space Flight Center, Huntsville, AL 35758, USA}

[3] {NASA Goddard Space Flight Center, Greenbelt, MD 20771, USA}

[4] {Science Systems and Applications, Inc, Lanham, MD 20709, USA}

[5] {JCET, University of Maryland – Baltimore County, Baltimore, MD 21228, USA}

[6] {SSEC, University of Wisconsin-Madison, WI 53707, USA}

[7] {NOAA Advanced Satellite Product Branch, Madison, WI 53707, USA}

Correspondence to: Pawan Gupta (pawan.gupta@nasa.gov)

Abstract

For nearly two decades we have been quantitatively observing the Earth's aerosol system from space at one or two times of the day by applying the Dark Target family of algorithms to polar-orbiting satellite sensors, particularly MODIS and VIIRS. With the launch of the Advanced Himawari Imager (AHI) and the Advanced Baseline Imagers (ABIs) into geosynchronous orbits, we have the new ability to expand temporal coverage of the traditional aerosol optical depth (AOD) to resolve the diurnal signature of aerosol loading during daylight hours. The Korean-United States – Air Quality (KORUS-AQ) campaign taking place in and around the Korean peninsula during May-June 2016 initiated a special processing of full disk AHI observations that allowed us to make a preliminary adoption of Dark Target aerosol algorithms to the wavelengths and

29   resolutions of AHI. Here, we describe the adaptation and show retrieval results from AHI

30   for this two-month period. The AHI-retrieved AOD is collocated in time and space with

31   existing AErosol RObotic NETwork stations across Asia and with collocated Terra- and

32   Aqua-MODIS retrievals. The new AHI AOD product matches AERONET, as well as

33   does the standard MODIS product, and the agreement between AHI and MODIS

34   retrieved AOD is excellent, as can be expected by maintaining consistency in algorithm

35   architecture and most algorithm assumptions. Furthermore, we show that the new product

36   approximates the AERONET-observed diurnal signature. Examining the diurnal patterns

37   of the new AHI AOD product we find specific areas over land where the diurnal signal is

38   spatially cohesive. For example, in Bangladesh the AOD increases by 0.50 from morning

39   to evening, and in northeast China the AOD decreases by 0.25. However, over open

40   ocean the observed diurnal cycle is driven by two artifacts, one associated with solar

41   zenith angles greater than 70° that may be caused by a radiative transfer model that does

42   not properly represent spherical Earth, and the other artifact associated with the fringes of

43   the 40° glint angle mask. This opportunity during KORUS-AQ provides encouragement

44   to move towards an operational Dark Target algorithm for AHI. Future work will need to

45   re-examine masking including snow mask, re-evaluate assumed aerosol models for

46   geosynchronous geometry, address the artifacts over the ocean and investigate size

47   parameter retrieval from the over ocean algorithm.

49   **1.0 Introduction**

50

51   Atmospheric aerosols, small liquid or solid particles suspended in the atmosphere, play a

52   key role in Earth's energy balance, cloud physics, geochemical cycles and air

53   quality/public health (Boucher et al., 2013; Rosenfeld et al., 2014ab; Seinfeld et al., 2016;

54   Jickells et al., 2005; Yu et al., 2015; Lim et al., 2012). These particles originate from both

55   human activity and natural processes, and they can cover vast regions of the globe.

56   Observations from satellite sensors provide the best means for monitoring and

57   quantifying the extent and transport of large-scale aerosol events (Kaufman et al., 2005;

58   Yu et al., 2012), and provide some characterization of aerosol particle properties (Remer

59   et al., 2005; Torres et al., 2013; Kalashnikova and Kahn, 2006; Kahn and Gaitley 2015).

60   Especially since the launch of NASA's Earth Observing System (EOS) and similar

61   satellites by international agencies, the community has benefitted from nearly two

62   decades of quantitative measures of the global aerosol system. While both passive and

63   active sensors have contributed to our understanding of the global aerosol system, here

64   we focus on only passive sensors. These, such as the MODerate resolution Imaging

65   Spectroradiometer (MODIS) (Levy et al., 2013; Hsu et al. 2013; Lyapustin et al., 2011),

66   the Multiangle Imaging Spectro-Radiometer (MISR) (Diner et al., 1998; Martonchik

67   1998; Kahn et al., 2010), the Ozone Monitoring Instrument (OMI) (Torres et al., 2013),

68   and POLarization and Directionality of the Earth's Reflectances (POLDER) (Tanré et al.,

69   2011) have provided instantaneous measures of aerosol loading, particle size, particle

70   absorption and aerosol type across the globe. The community has used these data to

71   calculate decadal statistics of aerosol climatology, seasonal and monthly statistics,

72   quantitative measures of intercontinental aerosol transport and fertilization of ecosystems

73   (Remer et al., 2008; Yu et al., 2012, 2013, 2015). These satellite aerosol products have

74   been used to estimate aerosol radiative effects and climate forcing, associations between

75   aerosols and cloud micro- and macrophysics, precipitation, air quality and public health,

76   and have provided critical constraints on global climate modeling (Zhang et al., 2005;

77   Koren et al. 2005; Lin et al. 2006; Wang and Christopher, 2003; Quaas et al., 2009;

78   Patadia et al., 2008; to give just one early example of each application).

79

80   The sensors mentioned above all have been launched on polar orbiting satellites in low

81   earth orbit (LEO). Such satellites are sun synchronous, passing over each location on

82   Earth at approximately the same local solar time each day. A LEO sensor imaging a

83   broad swath of Earth will image every spot on Earth, and thus achieve full global

84   coverage in 1 or 2 days. However, each spot on Earth is only viewed once per day in

85   daylight and once per day at night, always at approximately the same local solar time. In

86   contrast a geosynchronous (GEO) satellite orbits at a high altitude above Earth, matching

87   the same period as the Earth's rotation. A sensor on a GEO satellite can scan the full or

88   partial portion of Earth's face presenting to the satellite. Neither the sensor nor the Earth

89   appear to move in these images although the terminator between day and night on the

90   Earth appears to move from east to west across the image over time. A GEO imager

91 always views the same Earth locations across approximately 1/3 of the Earth, and cannot

92 by itself provide full global coverage. However, a sensor on a GEO satellite can provide

93 information on the aerosol in any viewed location as a function of time of the day,

94 enabling monitoring of the diurnal cycle.

95

96 For about a decade there has been a publicly available operational aerosol product

97 derived from a GEO sensor. This is the GOES Aerosol Smoke Product (GASP) (Prados

98 et al.,2007), where GOES stands for Geostationary Operational Environmental Satellite.

99 GASP provides aerosol optical depth for the daylight section of the continental United

100 States at 4 km spatial resolution every 30 minutes in near real time, and the data is

101 archived. The sensor has only five channels, one spectrally broad channel (0.52-0.71 μm)

102 in the visible and four in the near to thermal infrared. The aerosol retrieval algorithm

103 makes use of the infrared channels for cloud masking, but must acquire all of its aerosol

104 information from a single visible channel. The lack of a channel in the shortwave infrared

105 (e.g. 2.1 or 2.2 μm) prohibits application of an EOS-era Dark Target retrieval (Kaufman

106 et al., 1997; Levy et al., 2007) and the lack of any channel in the blue eliminates the

107 possibility of a Deep Blue retrieval (Hsu et al. 2004, 2013). Thus the GASP retrieval is

108 handicapped by the relative primitiveness of the GOES-13 sensor. Even so, aerosol

109 optical depth (AOD) retrievals from GASP collocated and compared with AOD

110 measurements from the AERosol Robotic NETwork (AERONET; Holben et al. 1998) at

111 10 sites in the northeastern U.S. and Canada showed reasonable agreement. Regression of

112 GASP and AERONET AOD derived correlation of 0.79, rms difference of 0.13, and

113 absolute bias of less than 30% for larger AOD (e.g. AOD > 0.1). Validation in the

114 southeast and western U.S. was less good. The GASP validation statistics are reasonable,

115 but not as good as those produced by MODIS AOD retrievals at the same AERONET

116 locations. The main point of GASP, though, is not its absolute accuracy, but that it

117 provides quantitative information on the diurnal cycle of aerosol across the continental

118 United States and southern Canada.

119

120 We are now entering a new era in GEO observations. With the launch of the Advanced

121 Himawari Imager (AHI) (Yu and Wu, 2016) and the Advanced Baseline Imager (ABI) on

122 GOES-16 and GOES-17 (Kalluri et al., 2018), we have sensors in GEO orbit with

123 spectral capability similar to MODIS. AHI has 16 bands, including three in the visible

124 and another in the SWIR. ABI also has 16 bands, but distributed differently across the

125 visible to the SWIR. This spectral capability combined with nominal spatial resolution

126 0.5 to 2 km creates opportunity for aerosol retrievals that can advance beyond what

127 GASP could produce. Aerosol algorithms developed and implemented by the agencies

128 responsible for the operations of the GEO satellites are or will be produced operationally

129 and made public. These include the Japanese Meteorological Agency (JMA) for AHI on

130 Himawari (Uesawa, 2016) and the National Oceanographic and Atmospheric Agency

131 (NOAA) for ABI on the GOES-R series. In addition to these official operational

132 products, other algorithms have been developed that make use of the new generation of

133 GEO observations for aerosol retrievals, especially for AHI data (Sekiyama et al., 2015;

134 Yumimoto et al., 2016; Lim et al., 2016, 2018ab; Zhang et al., 2018; Yoshida et al.,

135 2018;Yang et al., 2018; Shi et al., 2018; Yan et al., 2018). Some of these alternative

136 aerosol products are research algorithms for specific purposes, while others could be of

137 general interest and could be made public.

138

139 Because the capabilities of the new GEO sensors replicate the important spectral and

140 spatial capabilities of the MODIS sensors, the MODIS Dark Target (DT) algorithms over

141 land and ocean (Remer et al., 2005; Levy et al., 2010, 2015, 2018; Gupta et al., 2016) can

142 be applied to AHI or ABI observations with only minor adjustments. The expectation is

143 that the resulting aerosol product will match the original MODIS product in terms of

144 accuracy and availability (number of retrievals). More than providing just another

145 alternative aerosol product to the community, application of the traditional DT algorithm

146 to GEO sensors offers continuity with a nearly 20-year well-studied, validated, and

147 accepted aerosol product. The continuity of a DT AHI or ABI algorithm means that there

148 could be an accurate MODIS-like aerosol product that resolves the day time diurnal

149 cycle, providing a well-understood quantitative measure of aerosol loading at fine

150 temporal resolution at the large regional scale.

151

152 In this study we present the results of the first attempt at porting the MODIS DT aerosol
153 algorithm to the AHI sensor on the Himawari-8 geosynchronous satellite. The study
154 makes use of a special limited data set of AHI spectral reflectances, prepared for research
155 purposes during the KORUS-AQ field campaign during May-June 2016. The purpose of
156 this work is to test whether there is any skill in applying the DT to AHI, and whether the
157 goal of a continuous time series of retrieved AOD from MODIS to AHI has any
158 probability of success. Furthermore, the study will identify issues that arise from the new
159 geometry, and demonstrate the ability of the new sensor to resolve aerosol signals using
160 the DT algorithm that previous sensors could not.
161
162 The AHI inputs and the algorithm will be described in Section 2, with emphasis made on
163 how the AHI algorithm differs compared to the MODIS implementation. Section 3 will
164 present results and compare these with standard MODIS retrievals and collocated
165 ground-based observations. Section 4 will explore the AHI aerosol product's diurnal
166 cycle at AERONET stations for validation, and then question how well the diurnal mean
167 AOD inferred from once-a-day LEO observations compare with a truer diurnal mean
168 compared from observations made at finer temporal resolution. Finally, results will be
169 summarized and discussed in Section 5.
170
171 **2.0 Data and retrieval algorithm**
172
173 **2.1 AHI sensor characteristics**
174
175 The AHI was first launched on the Himawari-8 satellite in 2014 and became operational
176 in July 2015. It is in geosynchronous orbit over the equator at 140.7° East. The second
177 AHI was launched on the Himawari-9 in November 2016 and remains in a standby mode.
178 The instrument has the capability to image a mesoscale region every 30 seconds while
179 providing full disk coverage every 10 minutes. In this study, the full disk data have been
180 used. The data to be presented here were obtained from the University of Wisconsin
181 atmospheric Science Investigator lead Processing System (SIPS) which processed the
182 NOAA's operational cloud operating system – extended (CLAVR-x) which provides

183   radiance values at all 16 channels at a consistent 2km resolution as a

184   diagnostic/byproduct of the cloud retrieval. SIPS made the AHI data available

185   specifically to support the KORUS-AQ campaign and for research purposes, and thus

186   only two months of data were available. For this analysis we processed the DT algorithm

187   at 1-hour temporal resolution from 0000 UTC to 0800 UTC, 9 full disk images per day.

188   Figure 1 shows an example of the AHI full disk image. AHI wavelengths used in the DT

189   aerosol retrieval along with their spatial resolution are shown in Table 1, and compared

190   with their counterparts from the MODIS and Visible InfraRed Imaging Radiometer Suite

191   (VIIRS) instruments. From Table 1 we see that AHI nearly matches MODIS and VIIRS,

192   wavelength by wavelength in the bands needed by the DT algorithm, except for missing

193   the 1.24 µm band that is used in the aerosol retrieval over ocean and also in masking

194   snow/ice over land and sediments in the ocean. It is also missing the 1.38 µm channel

195   that the DT aerosol algorithm has relied on for identifying and masking thin cirrus. For

196   the bands that overlap MODIS, although close in spectral resolution, they do not exactly

197   match. For this reason the algorithm Look Up Tables (LUT), gas absorption corrections

198   etc. cannot be applied directly from the current MODIS algorithm and must be calculated

199   specifically for AHI.

200

201
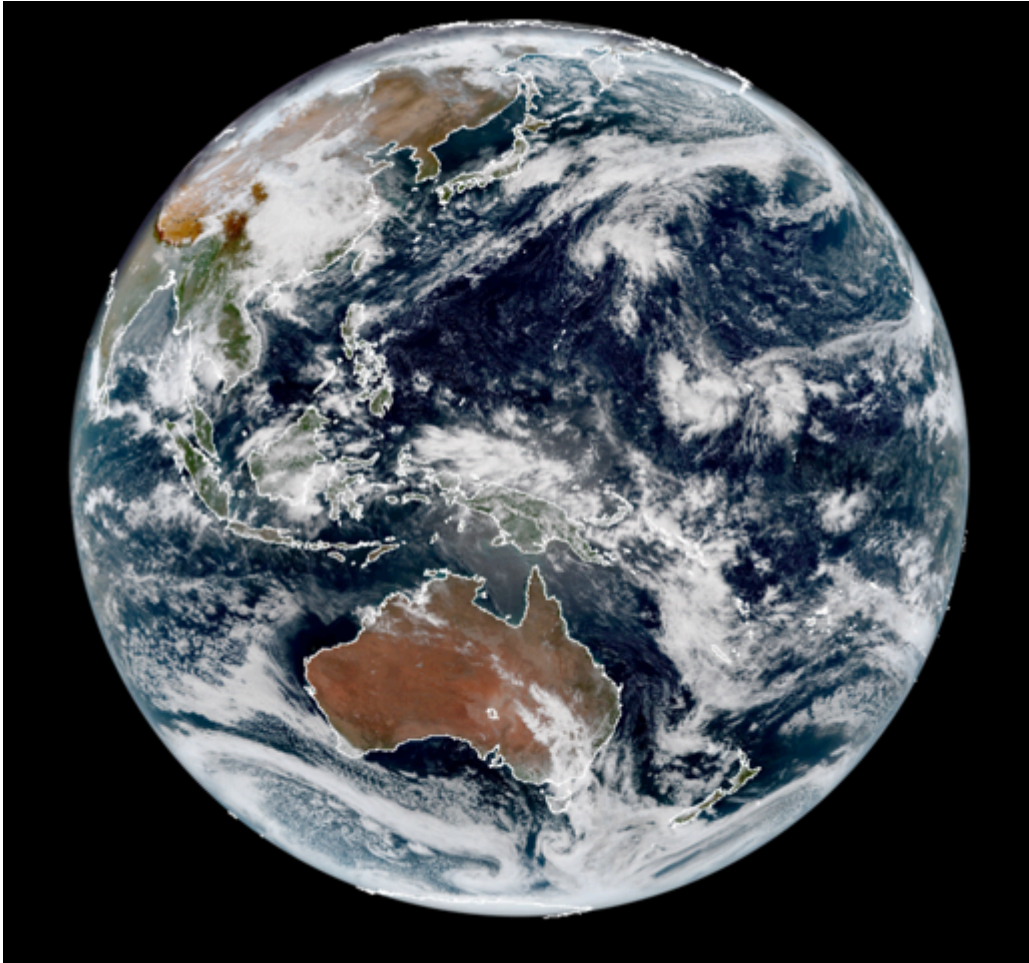
202 Figure 1. Full disk true color image from AHI using the 0.64 μm, 0.51 μm, 0.47 μm

203 channels. The image is taken on October 20, 2018 at 02:10 UTC.

204

205 AHI's native spatial resolution is coarser than MODIS's, but comparable to VIIRS. Note,

206 however, that the spatial resolution noted in Table 1 refers to the subsatellite point. The

207 spatial resolution of Earth scenes at the edges of MODIS and VIIRS swaths or at the edge

208 of the AHI disk will have spread from their subsatellite value. MODIS pixels spread by 4

209 times their nadir value, and VIIRS pixels spread by 2 times. AHI pixels remain 1-3 times

210 their size at the subsatellite point for all but the extreme edge of the full disk image. Also

211 note that the actual KORUS-AQ data used in this study have reduced spatial resolution in

212 all channels (2 km).

213

214

215

216 Table 1. MODIS, VIIRS and AHI wavelengths in μm used directly in the DT algorithm

217 (**bold**) and subsatellite point spatial resolution in kilometers. The table presents native

218 resolution of sensors, but this study uses a special run of AHI where all spectral channels

219 were reduced to a resolution of 2 km.

220

MODIS	VIIRS	AHI
0.47/0.5	**0.49**/0.75	**0.47**/1.0
0.55/0.5	**0.55**/0.75	**0.51**/1.0
0.66/0.25	**0.67**/0.75	**0.64**/0.5
0.86/0.25	**0.86**/0.75	**0.86**/1.0
1.24/0.5	**1.24**/0.75	
1.38/0.5	**1.38**/0.75	
1.61/0.5	**1.61**/0.75	**1.61**/2.0
2.11/0.5	**2.25**/0.75	**2.25**/2.0

230

231 Given that the wavelengths and spatial resolution of AHI differ from the heritage DT

232 aerosol algorithm means that while the structure, heritage and experience of the MODIS

233 DT algorithm can be adapted for AHI to maintain as much continuity as possible, the

234 resulting AHI algorithm and product will not be an identical twin.

235

236 **2.2 Dark Target AHI aerosol algorithm and research product**

237

238 The DT aerosol algorithms are a family of algorithms, based on the original two

239 algorithms that retrieved aerosol over ocean and over land from the MODIS instruments

240 aboard NASA's Terra and Aqua satellites. Levy et al. (2010, 2015, 2018) and the on-line

241 Algorithm Theoretical Basis Document (https://darktarget.gsfc.nasa.gov) describe these

242 algorithms in depth. Here we only provide an overview in order to highlight the

243 differences between the original algorithms and the DT algorithm applied to AHI inputs.

244 DT algorithms should not be confused with other operational NASA aerosol algorithms

245 applied to MODIS inputs (e.g. Deep Blue; Hsu et al., 2013 and MAIAC: Lyapustin et al.,

246   2011). Both DT ocean and DT land procedures use Lookup Tables (LUTs). LUTs are

247   created by using radiative transfer (RT) code to simulate spectral top-of-atmosphere

248   (TOA) reflectance for expected conditions of aerosols over a theoretical rough ocean

249   surface or black land surface. These LUTs assume intrinsic physical and optical

250   properties (size, shape, refractive index) as well as total column loading of atmospheric

251   aerosols.

252

253   The original DT retrieval relies on seven reflective solar bands for aerosol retrieval and

254   one for cirrus detection and masking (Table 1). Additional bands are used for tasks like

255   cloud masking, snow identification, etc. The algorithm adapted for AHI makes use of 6

256   bands for the aerosol retrieval that are similar, but not exactly the same as the original

257   MODIS ones. The differences require new corrections for trace gas absorption in the

258   channels, and the calculations of new LUTs. It is thus impossible to exactly duplicate the

259   DT algorithm as it is ported from sensor to sensor. However, the basic physical

260   assumptions, RT codes, algorithm architecture, and intrinsic physical, and optical

261   properties used to calculate the LUTs are the same in the AHI DT algorithm, as they are

262   in the current MODIS and VIIRS DT algorithms.

263

264   The greatest consequences to missing the 1.24 μm band is in sediment masking for ocean

265   and snow/ice masking for land. New techniques that compensate for the missing

266   information were applied to the AHI data. For sediment masking, we follow Li et al.

267   (2003) as is standard for the DT algorithm, but substitute the 1.61 channel for the

268   standard 1.24 μm channel. Physically this substitution should work, as both channels are

269   expected to be black in sea water, which provides the background from which sediments

270   are flagged, but the substitution has not been well-vetted. We have not yet devised a

271   substitute for the over land snow/ice mask. The data analyzed and shown here are from

272   May and June 2016, months when no snow is expected in the domain. Devising, testing

273   and implementing an AHI snow mask will be needed before the DT AHI algorithm can

274   be applied year round. In terms of the direct aerosol retrieval, the lack of the 1.24 μm

275   information only affects the over ocean algorithm slightly, as the information from the

276 0.86 μm and the two longer wavelengths compensate for its absence (Tanré et al., 1996;
277 1997).

278

279 The loss of the 1.38 μm channel may have more pronounced consequences as it proved to
280 be the first line of defense against thin cirrus contamination in the aerosol product (Gao
281 and Kaufman, 1995). In this initial adaptation of the algorithm to AHI we have not
282 implemented any alternative test for thin cirrus, and therefore cirrus contamination is
283 expected in the results shown here. For clouds other than thin cirrus, we apply an internal
284 cloud mask to the input radiances, similar to the traditional MODIS aerosol cloud mask.
285 This mask is based on spatial variability of groupings of 3x3 input radiance pixels
286 (Martins et al., 2002), and the same thresholds were used. However, while the MODIS
287 aerosol cloud mask also incorporates specific tests from the standard MODIS cloud mask
288 (MOD/MYD35: Frey et al. 2008) that are based on thermal infrared channels, those
289 products are not available for AHI. No direct substitution is employed to compensate.
290 The absence of these specific external cloud mask tests will mostly affect high cold cloud
291 identification, and again this suggests that the results shown here will be affected by
292 cirrus contamination. Because alternative methods have not been developed for masking
293 clouds, and the alternative method for identifying sediments has not been vetted to the
294 same extent as the original MODIS DT masking techniques, the possibility of
295 contamination from these features affecting the aerosol retrievals is higher than
296 expectations based on the MODIS heritage.

297

298 The traditional MODIS DT algorithm aggregates 20 x 20 pixels at 0.5 km resolution to
299 form a "retrieval box". These 400 pixels are screened for clouds, glint, sediments,
300 improper land surfaces and other elements. Then the remaining pixels that have escaped
301 the masking are sorted from high to low reflectance, and the darkest and brightest "good"
302 pixels are arbitrarily eliminated. Darkest is defined as the darkest 20% over land and 25%
303 over ocean. Brightest is defined as the brightest 50% over land and 25% over ocean. At
304 that point, the spectral reflectance from those pixels that remain after the 2-tiered
305 elimination process are averaged to represent the mean spectral reflectance in the nominal
306 10 x 10 km^2 retrieval box. The algorithm proceeds with the inversion using that

307   representative spectral reflectance and produces one set of aerosol properties

308   representative of the retrieval box.

309

310   The AHI retrieval algorithm adapts this MODIS process for its coarser spatial resolution

311   by aggregating 10 x 10 pixels at 2.0 km resolution to create retrieval boxes that have

312   nominal resolution of 20 x 20 km^2 (at the subsatellite point). The same 2-tier elimination

313   process using modified cloud, sediment, glint etc. masking, and removal of darkest and

314   brightest pixels is applied. Both the MODIS and AHI remove the same percentage of

315   dark and bright pixels. Because AHI starts the process with 100 pixels but MODIS with

316   400 pixels, there are fewer pixels to remove with AHI, and smaller number of pixels

317   remaining to be used to represent the spectral reflectance in the box with AHI. After the

318   representative reflectances have been calculated there are corrections for gas absorption

319   (H_2O, O_3, CO_2). The result is a single set of spectral reflectances in the six bands that is

320   input to the retrieval algorithm. Additional inputs include ancillary data such as ozone

321   profiles, wind speed and water vapor columns from NOAA's Global Data Assimilation

322   System (GDAS) reanalysis data, and a global land/sea mask generated by CLAVR-x at 2

323   km resolution.

324

325   Whether ocean or land, the DT retrieval searches the pre-computed LUTs to find the best

326   match to the spectral observations. The over land algorithm makes use of measured

327   reflectance at 0.47, 0.66 and 2.1 µm and assumptions about the surface reflectance to

328   determine the aerosol loading and establish the relative weights between two aerosol

329   models, both defined by geographical location and season. Over ocean, the algorithm

330   uses six wavelengths (0.55, 0.66, 0.86, 1.24, 1.61 and 2.13 µm) to determine the aerosol

331   loading and define an aerosol model from one fine mode and one coarse mode, and the

332   relative weight between these modes. There are no restrictions on the distribution of

333   modes by location and season in the ocean algorithm. Once the aerosol model is defined

334   by the weighting between models or modes, the spectral extinction of the aerosol is

335   defined. The retrieved aerosol loading can be translated to AOD at any wavelength

336   because of the known spectral extinction, and all wavelengths are reported in the output.

337   The primary wavelength we will use here is AOD at 0.55 µm. Two measures of aerosol

338 particle size are given for the over ocean retrieval, Fine Mode Weighting and Ångström

339 Exponent (AE). AHI-retrieved aerosol size parameters will not be examined in this paper.

340 Although the ocean and land retrievals have similarities, the details are different because

341 land surface optical properties are different than ocean. The ocean algorithm calculates a

342 "rough" surface (whitecaps, foam, glitter), which is a function of wind-speed, while the

343 land algorithm assumes quasi-static ratios between blue (0.47 μm), red (0.64 μm), and

344 shortwave infrared (e.g. 2.25 μm) wavelengths. Land surface ratios for the retrievals

345 shown in this study are identical to those used by the standard MODIS Collection 6.1

346 algorithm. Different wavelengths and different viewing geometry may introduce

347 unexpected uncertainties. Of particular concern is the assumption that LEO land surface

348 ratios will hold for the new GEO view geometry. Previously land surface ratios were

349 found to have only a weak dependence on the viewing geometry encountered by a LEO

350 observation (Levy et al., 2007), but the range of geometries encountered by a GEO

351 instrument are different and require further analysis. Still, the original assumption of

352 predictable surface reflectance ratios is based on the physical linkage between

353 chlorophyll and liquid water light absorption that should continue to transcend

354 Bidirectional Reflectance Distribution Function (BRDF) and other angular effects. In

355 addition to the aerosol properties, DT provides many diagnostics including Quality

356 Assurance and Confidence (QAC).

357

358 The new AHI DT algorithm was applied to input AHI full disk radiances, daylight

359 portion of the disk-only. View angles were confined to less than 72 degrees and solar

360 zenith angles were restricted to less than 80 degrees. The period of analysis spans two

361 months (May-June 2016). Given 9 images per day, the data base for analysis thus

362 includes more than 549 disk images of AOD derived from AHI inputs using the new AHI

363 DT algorithm.

364

365 **2.3 MODIS aerosol products**

366

367 The AOD retrieved from AHI using the DT retrieval will be compared with the more

368 established and well-characterized DT AOD product from MODIS on board the Terra

369 and Aqua satellites. Specifically we will be accessing Collection 6.1 Level 2 MOD04 and
370 MYD04 data products, where MOD refers to products derived from Terra MODIS inputs
371 and MYD refers to those derived from Aqua MODIS inputs. Level 2 refers to derived
372 geophysical parameters from the Level 1b geolocated and calibrated measured radiance
373 inputs. Level 2 data are provided in 5 minute cut sections of the orbital image called
374 granules. These images are not gridded, but instead follow directly from the instrument
375 scan as it follows its orbital path. There are many individual aerosol and diagnostic
376 parameters within each MOD/MYD04 file. This study makes use of only one parameter,
377 Optical_Depth_Land_And_Ocean. This parameter combines the retrieved AOD at 0.55
378 μm from the independent algorithms applied separately over land and ocean, and uses
379 only those retrievals identified with the highest quality (QAC=3 over land and QAC > 0
380 over ocean). MODIS granules were selected that fall within the daylight portion of the
381 AHI radiances, corresponding to the same days of the AHI images analyzed. Further
382 temporal (±0.5 hour) and spatial (0.25x0.25 degree) collocations have been performed for
383 specific analysis.
384
385 **2.4 AERONET aerosol products**
386
387 AERONET is a global ground network of CIMEL sun-sky radiometers and data processing
388 and analysis software commonly used to evaluate satellite-derived aerosol products
389 (Holben et al., 1998). In this work, only the direct sun measurements will be used.
390 AERONET processes these spectral measurements to derive AOD at the wavelengths
391 corresponding to the direct sun measurements. The AERONET spectral AOD product is a
392 community standard for satellite-derived AOD validation, given that AERONET's AOD
393 uncertainty of 0.01-0.02 (Eck et al., 1999) is sufficiently more accurate and precise than
394 can be expected by any satellite retrieval. The configuration of the spectral bands varies,
395 but typically is centered at 0.34, 0.38, 0.44, 0.50, 0.67, 0.87, and 1.02 μm. Here we use a
396 quadratic log-log fit (Eck et al., 1999) to interpolate AERONET AOD to 0.55 μm to match
397 the AHI AOD product. The typical temporal frequency of direct sun measurements is every
398 15 minutes. The network consists of hundreds of stations, located globally, across all
399 continents and in a wide variety of aerosol, meteorological and surface type conditions.

400   Here, we only include stations within the AHI view disk. AOD data from AERONET are

401   reported for three different quality levels: unscreened (level 1.0), cloud screened (level 1.5)

402   and cloud screened and quality assured (level 2.0). We will only use Version 3 Level 2.0

403   AERONET AODs in this study.

404

405   **3.0 Comparison with AERONET and MODIS DT**

406

407   The new AHI DT algorithm was applied to AHI-measured radiances over the full disk

408   (except for extreme viewing and solar angles), daily, through the 9 measurement times

409   (hourly: 0000 to 0800 UTC). We will test this new product by first validating it against

410   collocated AERONET measurements and then comparing it with the well-vetted MODIS

411   DT product.

412

413   **3.1 Validation against collocated AERONET AOD**

414

415   The validation procedure requires calculating the spatio-temporal statistics of a collocated

416   AHI-retrieved and AERONET-measured AOD pair (Ichoku et al. 2002; Petrenko et al.,

417   2012; Munchak et al., 2013; Remer et al., 2013, Gupta et al., 2018). Thus, the temporal

418   mean AOD of all AERONET AOD measurements within ±30 minutes of an AHI scan

419   will be compared with the spatial mean of all Level 2 AHI-retrieved AOD values within a

420   0.25x0.25 degree box centered at the AERONET station. This method of matching

421   spatio-temporal statistics, in one form or another, has become a standard within the

422   aerosol remote sensing community (Levy et al., 2010; Petrenko et al., 2012; Remer et al.,

423   2013, Huang et al., 2016, Gupta et al., 2018). As new satellite aerosol product types have

424   been introduced, the specifics of the spatio-temporal match-ups have been re-evaluated.

425   For example for the DT MODIS 3 km product different temporal and spatial averaging

426   windows were investigated, with smaller windows chosen to better test the ability of the

427   finer resolution product to capture spatial gradients at less than 10 km scales (Remer et

428   al., 2013). As the DT geosynchronous products mature, we will conduct a similar

429   investigation into better ways to validate the ability of the new products to represent the

430   immediate diurnal cycle of the AOD at an AERONET station. For now, our purpose is to

431   see if the product from ported the algorithm can match AERONET at a very basic level,

432   and we will use the standard match-up procedure at traditional scales. The validation

433   exercise with AERONET only considers AHI AODs pairs with highest quality AHI

434   retrievals.

435

436   From the collection of these ordered pairs of collocated AHI and AERONET AODs a set

437   of correlation and regression statistics will be calculated, assuming that the AERONET

438   AODs are the independent variables and the AHI AODs are the dependent variables.

439   These include number of AOD pairs (N), the correlation coefficient (R), the slope (m)

440   and intercept (I) of the linear regression through the points, the overall mean bias and

441   Root Mean Square Error (RMSE) of the AHI AODs. Also we apply the expected error

442   (EE), based on previous validation of MODIS DT AODs against collocated AERONET

443   (Levy et al., 2013). We show the percentage of AHI AODs that fall within the EE

444   bounds. EE gives us a sense of whether a new product is meeting the standards of the

445   original product, which in itself has become a standard within the aerosol remote sensing

446   community. Another metric that could be used would be the Global Climate Observing

447   System (GCOS) criteria for AOD, which is 0.03 or 10%. This is a more stringent

448   requirement than what we have been able to achieve with the DT algorithm applied to

449   MODIS for 20 years, or to VIIRS. Thus, the GCOS requirement is not shown on the

450   validation plots, as it is certainty out of reach for this first test of DT applied to a GEO

451   sensor.

452

453   Figure 2 shows the results of this validation for the over land retrieval, with Fig. 2a

454   showing the scatterplot of the accumulation of all collocations for the duration of the time

455   period investigated, and also specific panels showing the same, but for individual

456   AERONET sites. The specific stations were chosen to represent three different validation

457   situations: when DT is biased high, biased low and unbiased against AERONET. Figure

458   3 shows the validation statistics calculated for each AERONET location within the AHI

459   domain. Altogether there were 1982 collocations during the period of the study, with a

460   dynamic range spanning AERONET-measured AOD from less than 0.05 to nearly 2. The

461   AHI AODs match AERONET observations with a correlation coefficient of 0.84, a mean

462 bias of 0.09 and RMSE of 0.20. Approximately 55% of the retrievals fall within the EE
463 that was based on MODIS validation. Figure 3 shows that the distribution of validation
464 statistics varies from station to station, but that correlations tend to be overall high across
465 mainland Asia, while biases, RMSE and percent within MODIS DT Expected Error vary
466 more widely, even within tightly packed local networks. The variability in AHI AOD
467 performance against AERONET over the domains comes from various reasons, including
468 variations in surface reflectance characterization (i.e. different type of land use type),
469 variability in assumed aerosols models within the algorithm and availability of high
470 quality valid AOD retrievals over individual stations. Often AOD is biased high when
471 surface reflectance ratios do not conform to assumptions. Such was the case for many
472 years with urban surfaces, until Collection 6.1 made an alteration (Gupta et al. 2016).
473 Even with that alteration, DT retrievals over Beijing continue to be high (Figure 4). Low
474 biases will occur when the assumed aerosol model is underrepresenting the amount of
475 light absorption of the particles. The land aerosol model used in this region in this season
476 is the moderately absorbing aerosol in May and the non-absorbing model in June. If the
477 aerosols are actually absorbing in June or more heavily absorbing in May in a particular
478 locality, such as at KORUS_UNIST_Ulsan, then   the retrieved AOD will be biased low.
479 The DT algorithm is designed for global-scale representation of the aerosol system,
480 which for GEO means full disk retrievals. The goal is to provide the most accurate
481 retrieval at each individual location, but the reality is that on the global scale we cannot
482 fine-tune land surface and aerosol model assumptions for each individual location, and
483 some locations will have products that are biased high and some biased low.
484
485 As a comparison, Figure 4 shows a similar set of plots, but for MODIS DT retrievals
486 against AERONET. These collocations were made at the same stations as in Fig. 2, and
487 over the same time period. Both Terra and Aqua are included. First, we see about half as
488 many points as were seen in the AHI collocations because Terra and Aqua MODIS each
489 pass over the area only once per day during daylight hours, while AHI is scanning these
490 sites up to 9 times per day. Second, we notice that MODIS AODs match collocated
491 AERONET AODs about the same as AHI AODs with R = 0.91, bias = 0.10, RMSE =

492   0.19, and with 55% within EE. Only the correlation between MODIS and AERONET is

493   substantially better than between AHI and AERONET.

494

495   We see from this limited validation that the AHI-retrieved AOD is sufficiently accurate

496   to represent the aerosol in this region, during this time period, approaching the same

497   validation statistics as the durable MODIS product. Additional analysis of AHI AOD

498   biases as a function of surface reflectance, aerosol typing, season, and sensor and satellite

499   geometry required data covering a longer time period. We plan to perform a more robust

500   analysis in our ongoing and future research before making the product operational. We

501   will next compare the full overlap of AHI-retrieved AOD with MODIS retrievals,

502   regardless of AERONET.

503

504
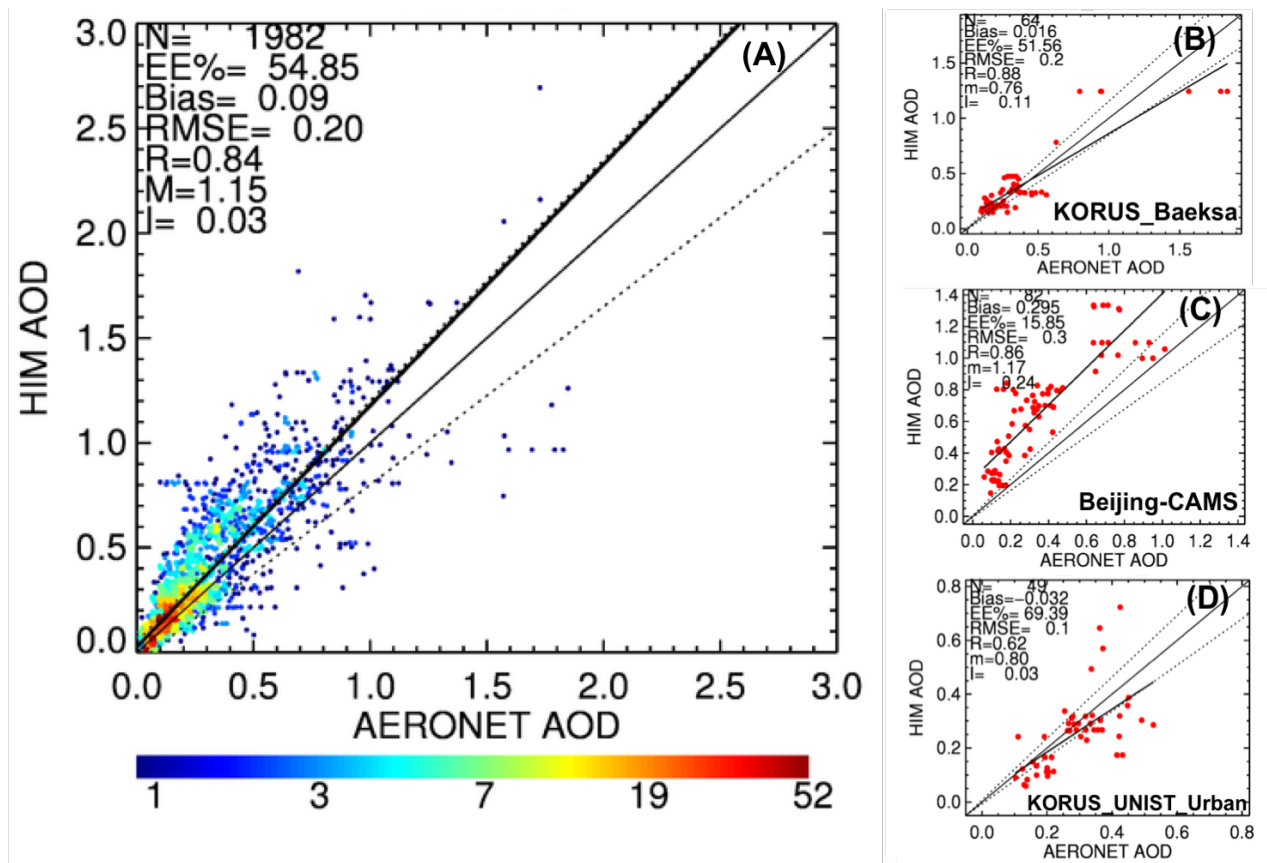
505   Figure 2. Density scatterplots of retrieved AOD at 550 nm derived from AHI radiances

506   using the new DT AHI algorithm versus AOD at 550 nm spectrally interpolated from

507   measured AODs from AERONET instruments collocated in time and space. Left panel

508   A. All accumulated collocations in the AHI full disk domain over the 2 months study

509   period May-June 2016. Right panels B, C and D, same for individual stations KORUS-

510   Baeksa and KORUS-UNIST_Ulsan in Korea and Beijing-CAMS in China. Shown in

511   each panel are the number of collocations (N), percent within expected error as

512   determined from MODIS DT analysis (EE%), mean bias (Bias), Root Mean Square Error

513   (RMSE), correlation coefficient (R), slope (m) and intercept (I) of a linear regression

514   equation through the points.

515

516
517
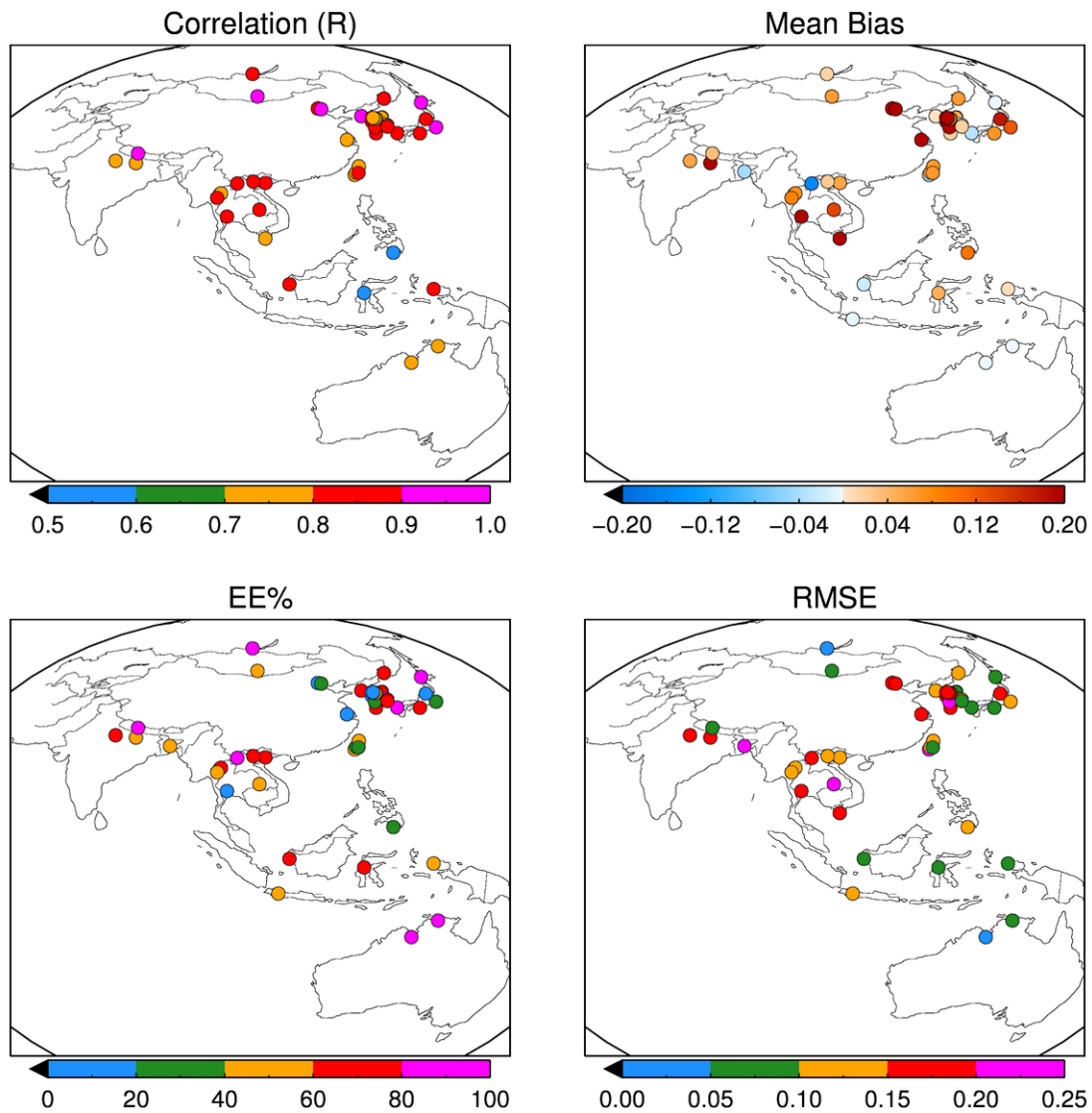
518   Figure 3. Spatial distribution of the collocation statistics between retrieved AOD at 550

519   nm derived from AHI radiances using the new DT AHI algorithm versus AOD at 550 nm

520   spectrally interpolated from measured AODs from AERONET instruments collocated in

521   time and space. Shown are upper left: correlation (R); upper right: mean bias; lower left:

522   Percentage within expected error (EE%); lower right: RMSE. Each point represents an

523   AERONET station location.

524

525
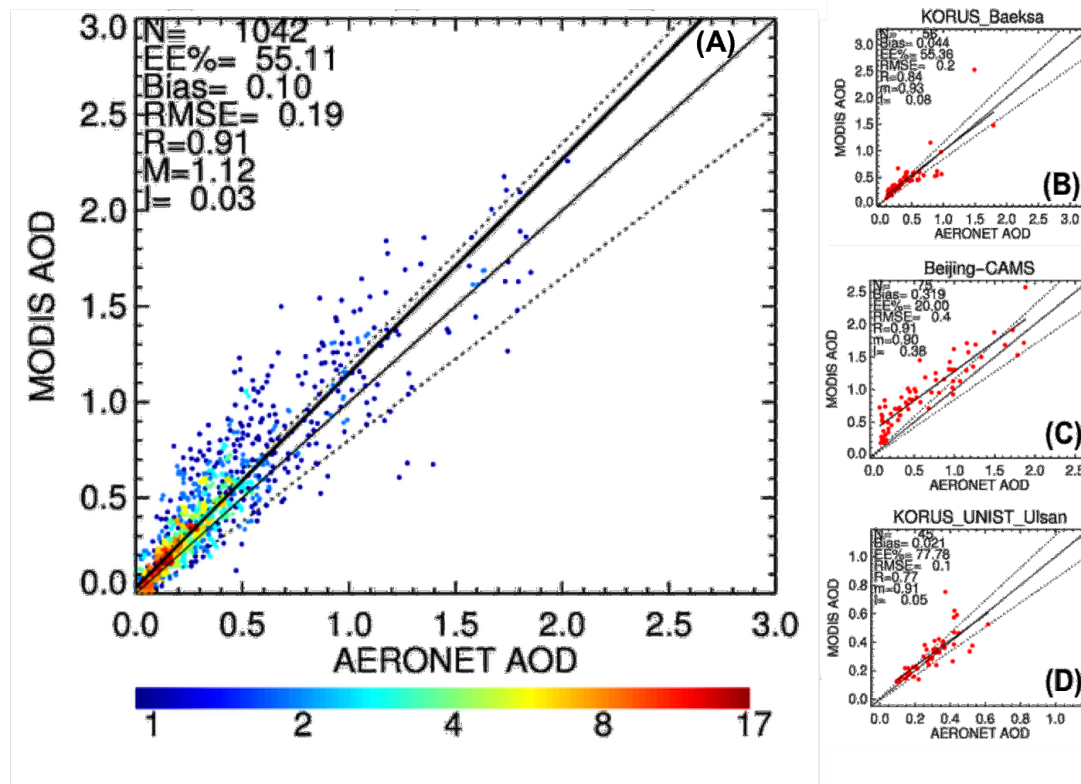
526   Figure 4. Same as Figure 2 except now density scatterplots of retrieved AOD at 550 nm

527   derived from Terra and Aqua MODIS using the operational DT Collection 6.1 algorithm.

528   This data represents same stations and time period as shown in Fig2.

529

530   **3.2 AHI versus MODIS DT**

531

532   To collocate AHI and MODIS AOD, the Level 2 MODIS and AHI AOD data were

533   mapped to a common 0.25º latitude by 0.25º longitude grid for each AHI full disk scan.

534   To fill the grid, we include all MODIS retrievals within ±30 minutes of the AHI scan. All

535 the AOD retrievals falling within the above spatial and temporal windows were averaged

536 and statistics are retained for further analysis. It takes MODIS approximately 35-45

537 minutes to cut a poleward-to-poleward swath across an AHI image, and about 6-7 swaths

538 to transverse east-west across the disk. Thus, in the common grid, at any particular time,

539 while most of the grid has the possibility to include an AHI retrieval when cloud and glint

540 free, only a relatively small portion of the grid will be filled with MODIS retrievals to

541 create the possibility of a collocation.

542

543 Figure 5 presents the scatter plots from matching the products of the Terra/Aqua and AHI

544 sensors on the common grid in each subset. Terra and Aqua collocations are kept

545 separate, as are over land and over ocean retrievals. The DT AHI-retrieved AOD and the

546 DT MODIS-retrieved AOD exhibit excellent correlation and similarity, as is expected

547 from applying nearly the same retrieval algorithm to the radiance measurements of both

548 sensors. Over ocean there are over 600,000 match-ups for Terra and over 1 million for

549 Aqua. The geosynchronous AHI retrievals match the polar-orbiting MODIS retrievals

550 with essentially zero bias and RMSE of 0.05 or less. Correlation between the two data

551 sets is 0.93 or greater. Over land, there are over 100,000 match-ups for each satellite with

552 no bias for Terra and 0.02 for Aqua, and RMSE of 0.09 or less. Correlations exceed 0.95

553 over dynamic ranges from 0.0 to approximately 2.0. The plots in Figure 5 show how well

554 the new AHI-retrieved AOD matches its MODIS counterpart when both AHI and

555 MODIS offer retrievals for a particular time and location. These plots do not address

556 situations in which a retrieval occurs for one satellite, but not the other, and therefore do

557 not address typical retrieval issues such as cloud masking and choosing appropriate

558 situations for the DT algorithm to make a retrieval. There can be also differences in

559 AODs from two sensors due to difference in their viewing geometries. This is something

560 beyond the scope of this paper and will be addressed in subsequent research.

561
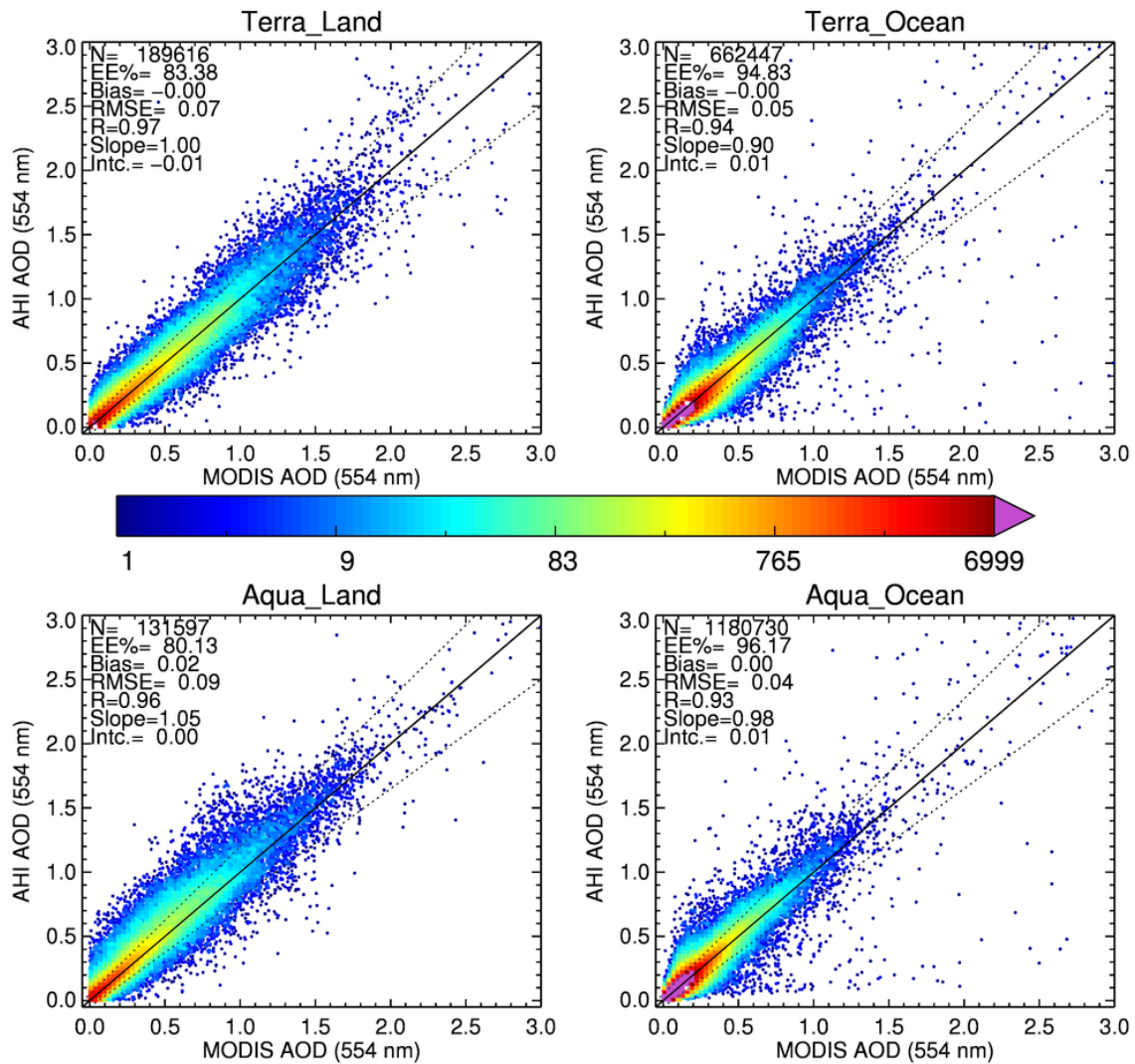
Figure 5. Density scatterplots of retrieved AOD at 554 nm derived from AHI radiances using the new DT AHI algorithm versus retrieved AOD at 554 nm from the operational MODIS Collection 6.1 algorithm, collocated in time and space. Top row are Terra MODIS. Bottom row are Aqua MODIS. Left panels are results from the over land retrieval. Right panels are results from the over ocean retrieval. The same collocation statistics are displayed as in Figure 2.

Figure 6 shows the two-month mean AOD over the AHI disk from AHI and Aqua MODIS, calculated from the data mapped to the common grid during our study period.

572 The mean AODs plotted here are collocated, and represent the AHI-derived AOD at
573 approximately the same time as the MODIS overpass.
574
575 We see that the DT algorithm applied to both sensors results in very similar distributions
576 of mean AOD across the AHI full disk image (Figure 6). This is despite the different
577 sensor characteristics and very different viewing geometries. There is elevated aerosol
578 across south and southeast Asia, and a separate pocket of elevated aerosol in northeast
579 China. Low AOD occurs across most of the tropical and southern oceans. Australia is
580 very clean and both sensors show a bit of moderately elevated AODs over the Indonesian
581 island of Java. The magnitude of mean AOD in these images ranges from near 0.0 to
582 almost 1.0.
583
584 The bottom panels of Figure 6 show the absolute differences in AOD when subtracting
585 the top row MODIS panel from the top row AHI panel, and a similar difference map
586 showing the differences between the top panel AHI values and a similar MODIS plot, but
587 from the Terra satellite. The difference maps are AHI minus MODIS so that positive
588 values, in red, indicate that AHI is higher than MODIS, while the negative values, in
589 blue, indicate that AHI is lower than MODIS. The range of differences span +0.10 to
590 about -0.08.
591
592 These plots indicate that over the elevated AOD regions, AHI retrievals are higher than
593 MODIS retrievals by as much as 0.10. This higher AHI AOD is more prevalent and
594 widespread with MODIS Aqua than with MODIS Terra. AHI tends to be about 0.02 to
595 0.03 higher than MODIS Aqua over much of the ocean regions surrounding the Asian
596 and maritime continents, while AHI tends to be closer to MODIS Terra in these regions
597 and sometimes even negative. Over Australia, AHI is less than MODIS Terra by as much
598 as -0.08. Because AOD values over Australia are very low to begin with, this negative
599 with respect to MODIS Terra indicates that AHI retrievals over Australia are often
600 absolutely negative more consistently than the MODIS retrievals and suggest that some
601 adjustment to the surface parameterization in the AHI DT retrieval will be required.
602

603   The inconsistencies between the two difference maps, one showing AHI with respect to

604   MODIS Aqua and the other with respect to MODIS Terra highlight the difficulty in

605   producing consistent representations of the AOD field, even when applying the same

606   algorithm to different sensors that should be exact duplicates of each other as in the case

607   of MODIS Terra and MODIS Aqua (Levy et al., 2018). Given this inconsistency between

608   the two MODIS instruments, the differences between AHI results and both MODIS

609   instruments fall within expected and manageable ranges. The DT algorithm as applied to

610   AHI is producing a representation of the spatial distribution of AOD with the same level

611   of fidelity as the original DT MODIS algorithm. This is the first attempt of applying the

612   DT algorithm to AHI, and we expect that future refinements to algorithm assumptions

613   that account for specific instrument characteristics and calibration will bring AHI AOD

614   results even closer to MODIS and AERONET values of AOD.

615

616

617

618
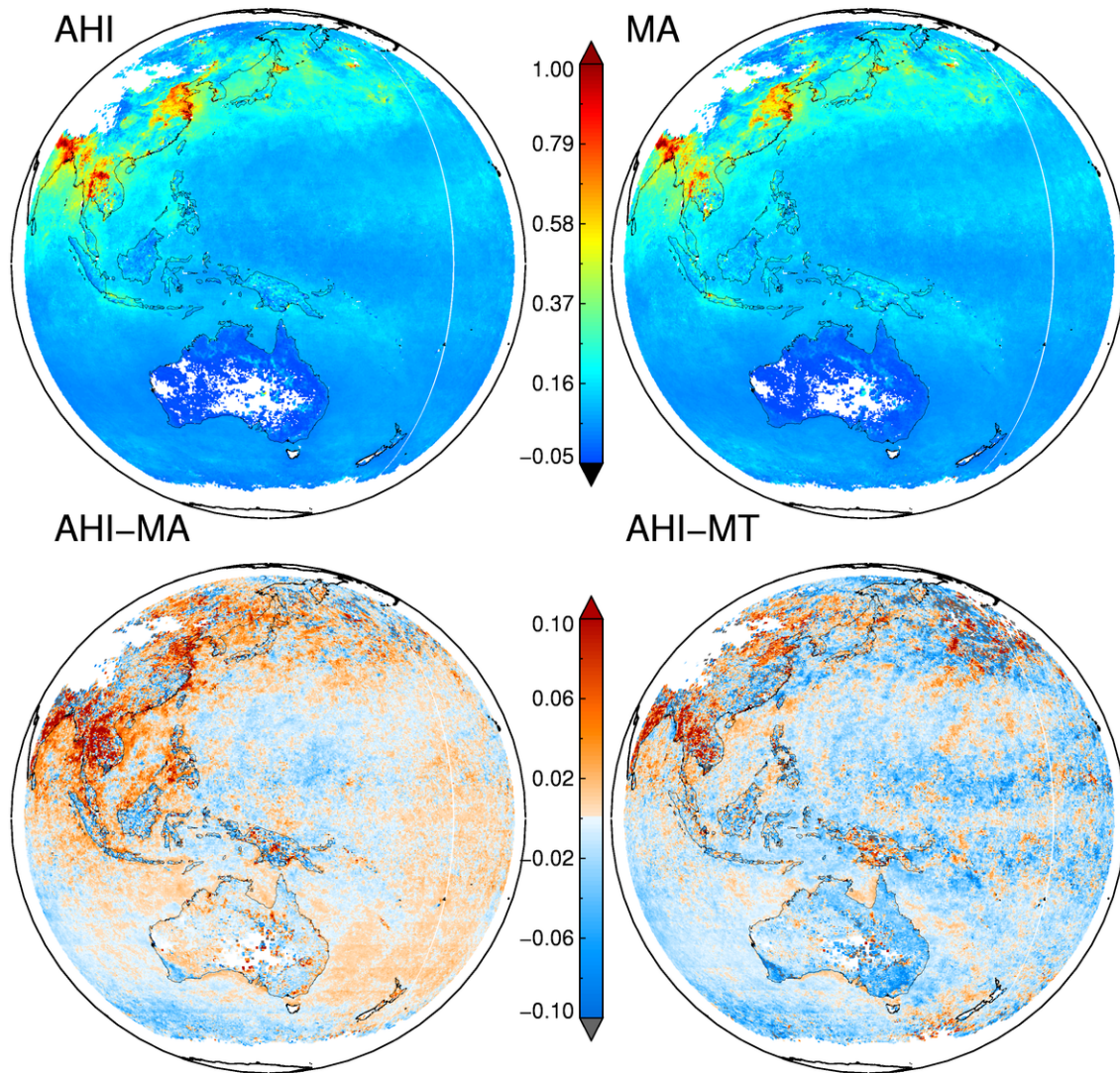
Figure 6. Top row: Mean AOD at 550 nm over the 2-month study period of May-June

2016. Upper left: mean AOD derived from retrievals using the new DT AHI algorithm

applied to AHI. Upper right: mean AOD derived from the standard Aqua MODIS DT

product. Bottom row: Difference maps of mean AOD at 550. Bottom left: Difference

between the two maps in the top row. Bottom right: Similar difference map but between

AOD from AHI and AOD from Terra MODIS (MT), instead of Aqua MODIS (MA).

625

626

627

628

4.0 Representation of AOD diurnal cycle using DT algorithm

4.1 Comparing AHI-derived diurnal signatures with AERONET

In the previous section we show how well the new DT AHI algorithm matches the AOD measurements from AERONET and the retrievals from MODIS. However, the point of applying an aerosol retrieval algorithm to a geosynchronous satellite sensor such as AHI is not to match the individual station data of AERONET nor the once-per-day retrievals from MODIS. The point of porting the DT aerosol algorithm to AHI is to represent the diurnal cycle of AOD over the broad regional area covered by the AHI full disk. In this section we explore the diurnal cycle of AOD derived from AHI and evaluate how much of the aerosol system MODIS has been missing because of its limited temporal sampling.

The diurnal cycle of AHI-derived AOD is compared with collocated diurnal patterns of AOD exhibited by AERONET stations within the AHI full disk image. The diurnal cycle at each AERONET station was calculated by finding the mean AERONET AOD at seven specific times of the day corresponding to the time of an AHI scan. These times are 01:00, 02:00, 03:00, 04:00, 05:00, 06:00 and 07:00 UTC, corresponding to the hours of 10:00 to 16:00 in local Korean time. All AERONET AOD measurements ±30 minutes of the nominal time were included in the average to represent the mean AOD at the nominal time. In parallel, the mean AOD at these specific times were calculated from all high quality AHI-derived level 2 AOD located within a 0.25x0.25 degree box centered around the AERONET station for all AHI scans taken at the nominal time. Thus, we created two representations of the diurnal cycle of AOD at each AERONET station, one from AERONET data and one from AHI-derived data, all from the collocation data set. This means that both AERONET and AHI must report at the same specific time for the instruments' AOD to be included in the calculated hourly average. This is the purest means to compare the actual retrieval, but will not reveal differences in sampling factors such as cloud masking because AHI will benefit from AERONET's cloud identification.

660
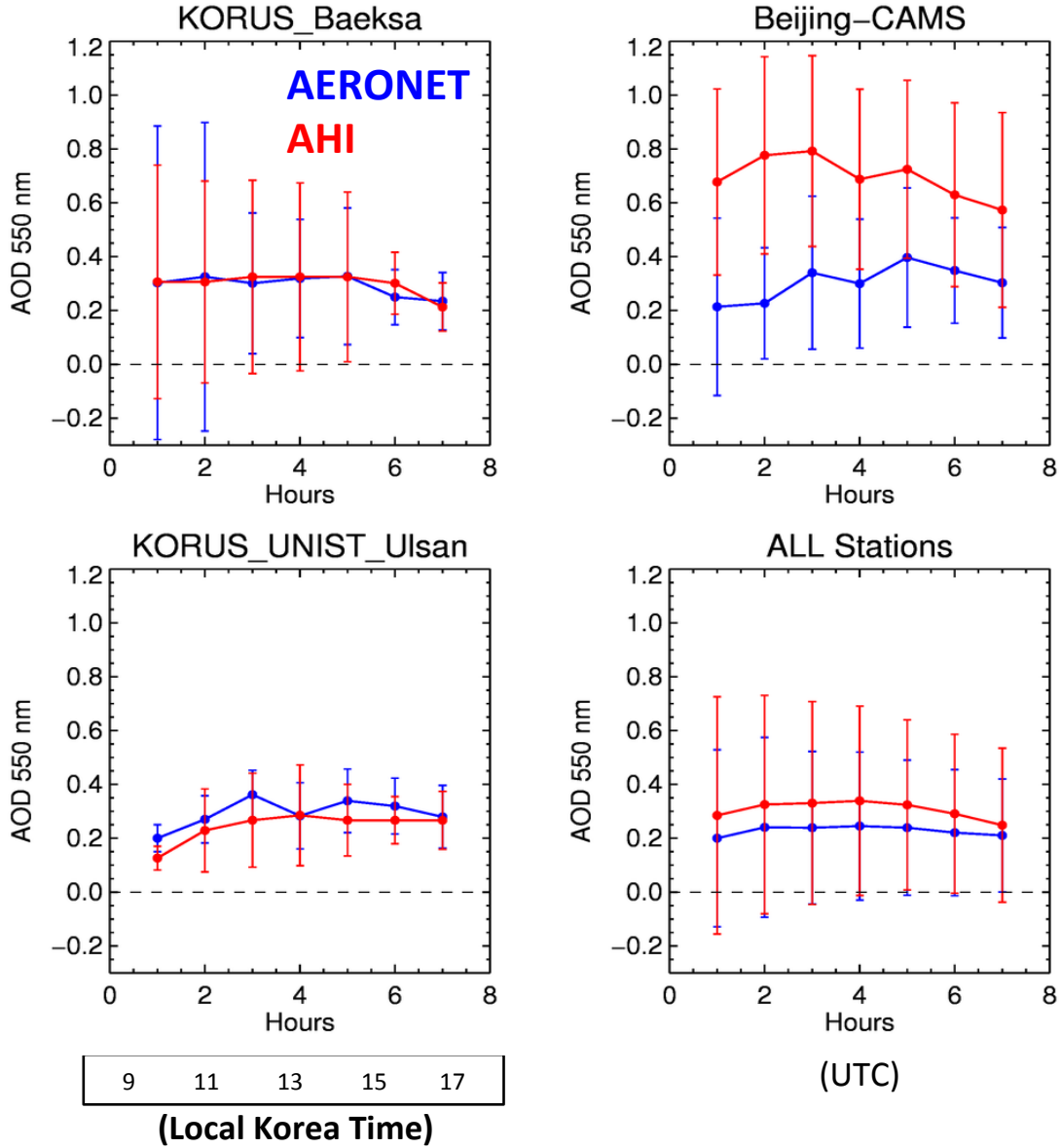
Figure 7. Median AOD at 550 nm in each of 7 time-of-day bins corresponding to 10:00 to
16:00 Korean standard time. Shown are three individual AERONET stations and also
(lower right) the results of binning all of the AERONET stations across the full disk
image as shown in Figure 3. Red indicates AOD derived from AHI using the new DT
algorithm. Blue indicates AOD measured by AERONET. The statistics were calculated
from the collocation data base such that each bin contains the same number of
observations from AHI and AERONET taken at the same time, although the number of
observations in each diurnal bin will differ. Vertical error bars represent one standard
deviation among different days for the same hour.

670 Figure 7 shows the calculated median AOD diurnal cycles from AERONET and AHI-

671 retrievals for three individual stations in Korea and China, and also the median of all

672 stations located in the AHI full disk image and reporting during our period of study. Error

673 bars represent the standard deviation of the sample in each hourly bin. At the three

674 stations shown individually in Figure 7, we see that the same biases seen in Figure 2 also

675 appear here, particularly with Beijing CAMS showing a strong positive bias. There is

676 wide scatter in the AOD for each hourly bin, as portrayed by the relatively large error

677 bars. The diurnal pattern of AOD, as measured by AERONET at KORUS Baeksa shows

678 a sudden decrease after 0500 UTC (14:00 Korea Standard Time), dropping from a steady

679 0.3 to 0.2 in two hours. The AHI AOD retrievals match this pattern almost exactly. The

680 other Korean station, KORUS_UNIST_Ulsan, shows an opposite daily pattern, with

681 AOD increasing from a morning low of 0.2 at 0100 UTC (10:00 Korean Standard Time)

682 to 0.3-0.4 at midday and then a drop off towards evening. The AHI AOD at this station is

683 biased low throughout most of the day, but does reflect the same diurnal signature of

684 increasing AOD over the morning. At the third station, Beijing CAMS, the AHI AOD

685 diurnal pattern does not match AERONET as well, but there is a strong positive bias

686 there with very large scatter in each hour. With error bars spanning 0.5 AOD, it is

687 difficult to discern diurnal changes with amplitudes of 0.2 AOD or less in either

688 AERONET or AHI.

689

690 The diurnal analysis shown in Figure 7 suffers from relatively small data samples. The

691 number of collocations for KORUS_Baeksa, KORUS_UNIST_Ulsan and

692 Beijing_CAMS are 56, 45 and 75, respectively, distributed over 7 hourly bins. If clouds

693 were not a factor, each hourly bin median might be constructed from only 6 to 11

694 samples. However, clouds are indeed a factor, with their own diurnal patterns. The actual

695 number of AHI-AERONET collocations at any particular hour might be as few as 3, and

696 morning and afternoon bins reported in Figure 7 might be constructed from entirely

697 different days. Therefore, the diurnal patterns in Figure 7 may be artificial composites

698 and not representative of the actual changes in AOD over the course of a single day.

699 However, the point of this comparison is not to speculate on the cause of the diurnal

700 signatures, but to establish that the AHI-derived AOD has the ability to describe the same
701 mean diurnal pattern in the aerosol as AERONET for individual locations.

702

703
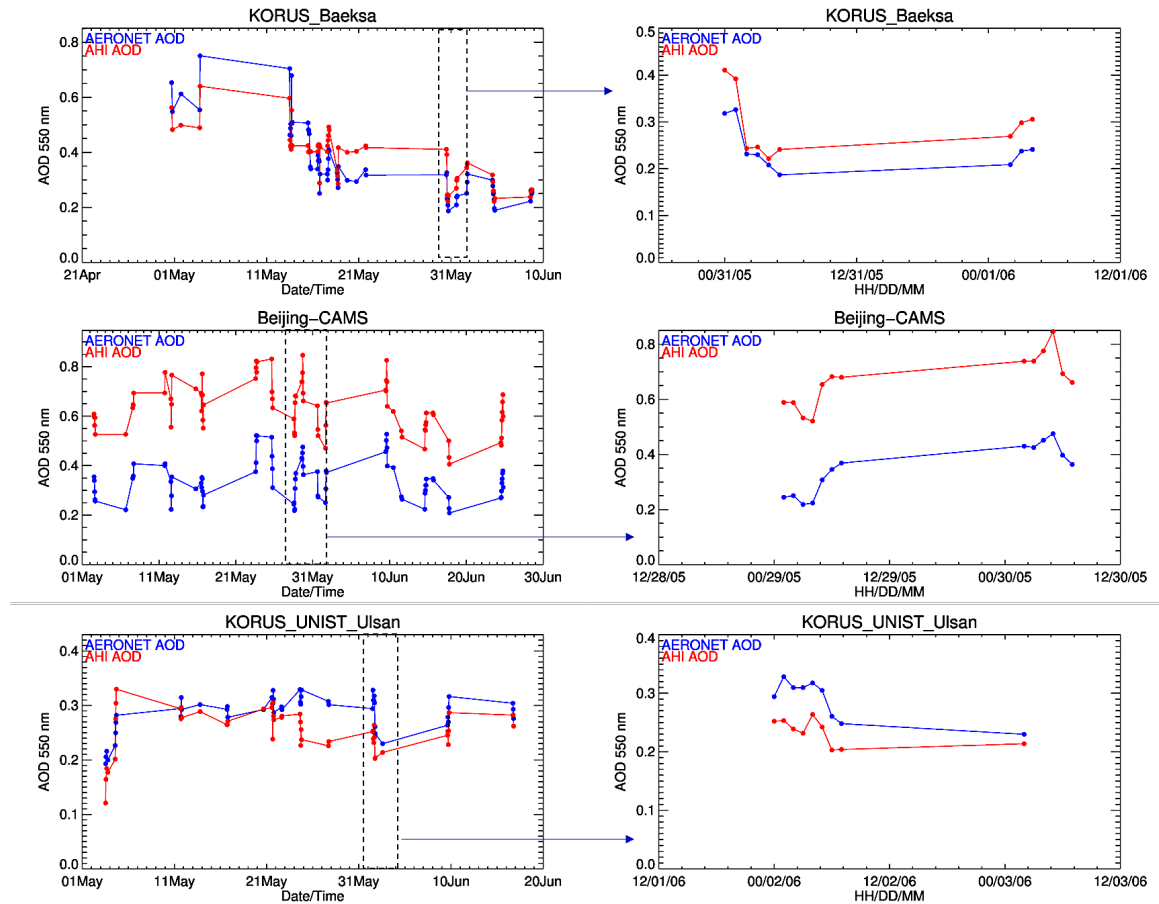
704 Figure 8. The time series of spatio-temporal mean AODs from AERONET (blue) and
705 AHI (red) for each hour of observation during the KORUS-AQ field campaign for the
706 same three stations as shown in Figure 7 (left panels). The right panels zoom into
707 selected days as shown in the box with dotted lines in the left panels for each station.

708

709 Figure 8 further demonstrates the capability of AHI retrieved AODs to represents realistic
710 diurnal cycles over these three stations on individual days rather than in average sense as
711 shown in Figure 7. This analysis shows that AHI retrieved AODs follows AERONET
712 AODs hour-by-hour and day-by-day with apparent positive and negative biases over
713 different stations as discussed in the earlier section. Additional KORUS-AQ time series

714 of AHI and AERONET AOD for 46 other stations are shown in the Supplemental

715 Material. While there are some stations where AHI AOD does not follow the AERONET

716 temporal variability as well as those shown in Figure 8, most do.

717

718 The ensemble statistics of the diurnal signature for all AERONET stations and collocated

719 AHI retrievals in the AHI full disk image show the high bias of the AHI retrievals, as per

720 Figure 2, but also that the ensemble mean diurnal signature of AHI AOD is mostly flat, as

721 is the diurnal signature from AERONET. Both AHI and AERONET AOD exhibit a slight

722 increase in AOD from morning to midday. Then, AHI decreases towards the end of the

723 day, while AERONET stays flat. The scatter in each hourly bin is large, as shown by

724 error bars that span 0.6 in AOD, and thus diurnal patterns with amplitudes of 0.1,

725 exhibited by both AHI and AERONET fall well below a significant signal to noise

726 threshold. Still the basic agreement of AHI to AERONET in the overall ensemble diurnal

727 statistics and in the individual time series comparisons is encouraging.

728

729 **4.2 Full disk AHI-derived AOD diurnal cycle**

730

731 Previously, Figure 6 showed the mean full disk AHI AOD calculated for the approximate

732 times of the MODIS overpasses. Now we calculate the overall mean AHI-derived AOD

733 calculated over the entire day light diurnal cycle and not just at MODIS overpass time,

734 for the duration of our study period at each of the 0.25^o latitude by 0.25^o longitude grid

735 squares. Figure 9 shows this overall period mean map, with all diurnal information lost.

736 The period mean map at MODIS overpass time (Figure 6) looks qualitatively very similar

737 to the overall period mean map (Figure 9), suggesting that MODIS sampling provides a

738 good representation of the overall AOD distribution.

739

740

741

742

743

744

745

746

747

748

749

750

751

752

753

754

755

756

757
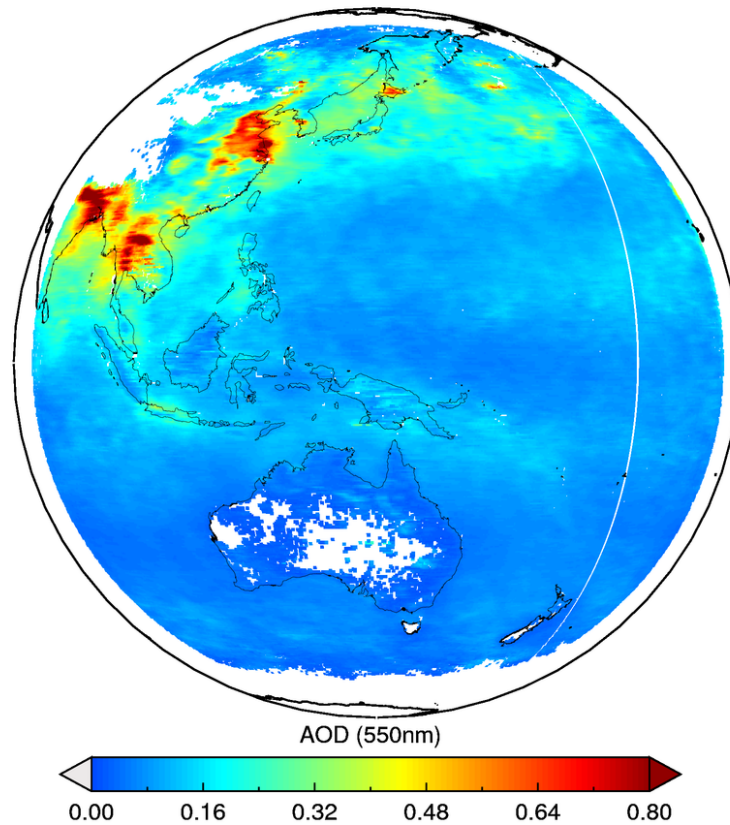
Figure 9 Daily mean AOD at 550 nm calculated over all daylight full disk images of AHI during May-June 2016. No requirements of collocation with MODIS or AERONET were imposed.

Then we calculate the mean AOD for each AHI full disk scan corresponding to a particular UTC hour, in each grid over the period of our study. Figure 10 shows the plots of the absolute difference (mean hourly AOD minus mean daily AOD) at each of these diurnal hours.

Figure 10 captures the diurnal signature of the aerosol over a broad region of Earth. Red colors indicate that at a particular hour of the day, the AOD is higher than the daily mean. Blue colors indicate that the hourly AOD is lower than the daily mean. The large gray circle that traverses the image from hour to hour is the glint mask preventing the over ocean algorithm from retrieving an AOD value. The glint mask is set for glint angles <

772   40º, which unfortunately eliminates large portions of a geosynchronous image from being

773   suitable for a DT aerosol retrieval. The glint mask proceeds across the image hour by

774   hour so that the glint mask becomes indiscernible in the daily mean. That is why there is

775   no apparent glint mask in the overall daily average of Figure 9, nor in Figure 6

776   constructed from AHI AOD collocated with MODIS. Continents and islands within the

777   glint mask will call on the over land DT algorithm that does not mask for glint, and

778   therefore, will return an AOD value.

779

780   The most striking feature in Figure 10 is the blue shading at the edges of the over ocean

781   retrieval domains that begin the day to the west in the Indian Ocean and then switch to

782   the east in the Pacific in the afternoon. This band of "lower than daily average" AOD is

783   associated with solar zenith angle, not view angle, as it hugs the day/night terminator in

784   the images, even when that terminator crosses the center of the full disk image. By 0700

785   and 0800 UTC, the terminator artifact encompasses a broad geographical swath of ocean,

786   which would introduce an incorrect interpretation of local diurnal AOD signal with

787   amplitudes of 0.15, when daily mean values are only 0.10. Such strong diurnal swings in

788   AOD over the remote ocean on global scales are unrealistic.

789

790   The problem may be introduced by the radiative transfer code used to create the Look Up

791   Tables for the over ocean retrieval (Ahmad and Fraser, 1982) that does not fully account

792   for Earth's curvature. Although this code has served the DT retrieval well through the

793   MODIS and VIIRs eras, those polar orbiting satellites only encounter extreme solar

794   zenith angles at the beginning and end of their orbits near the poles, where DT aerosol

795   retrievals are rare due to other factors such as extreme cloudiness or snow/ice. The

796   inability to properly model Earth's sphericity is likely to be of greater concern for

797   geosynchronous satellites that encounter extreme solar zenith angles across all latitudes

798   and in prime retrieval areas. See Figure 11. Currently the AHI DT algorithm retrieves all

799   geometries with solar zenith angle < 80 degrees. Figures 10 and 11 suggest that the

800   terminator artifact could be mitigated by applying a more stringent threshold of 70

801   degrees. However, development and application of a spherical radiative transfer code is

802   the more satisfying long-term solution.

AOD (Hourly–Daily)
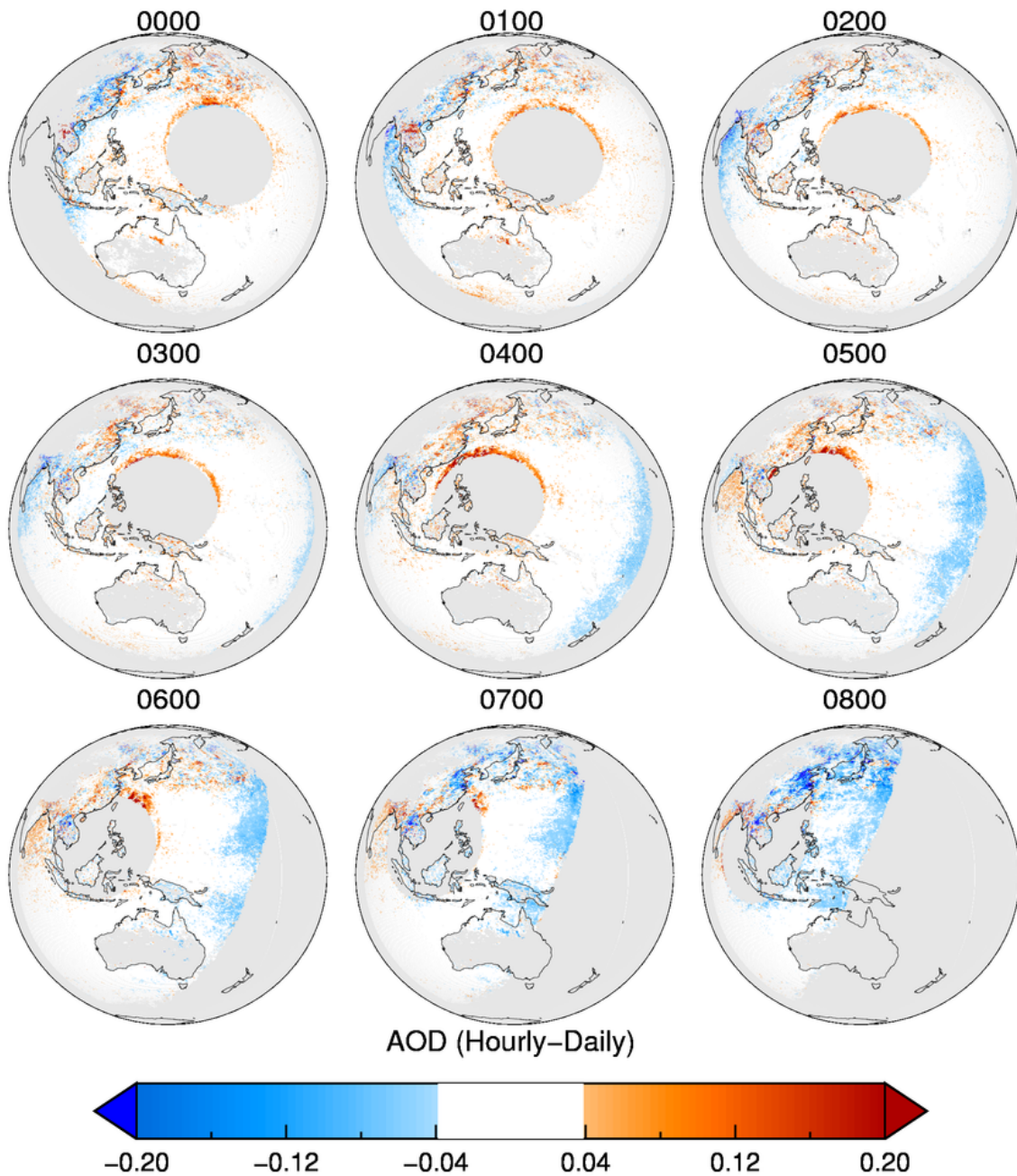
Figure 10. Difference in hourly mean AOD at 550 nm as derived from the new DT AHI

algorithm from the daily mean AOD, as plotted in Figure 8. Red indicates the specific

hour has higher AOD than the daily mean, and blue indicates the opposite.
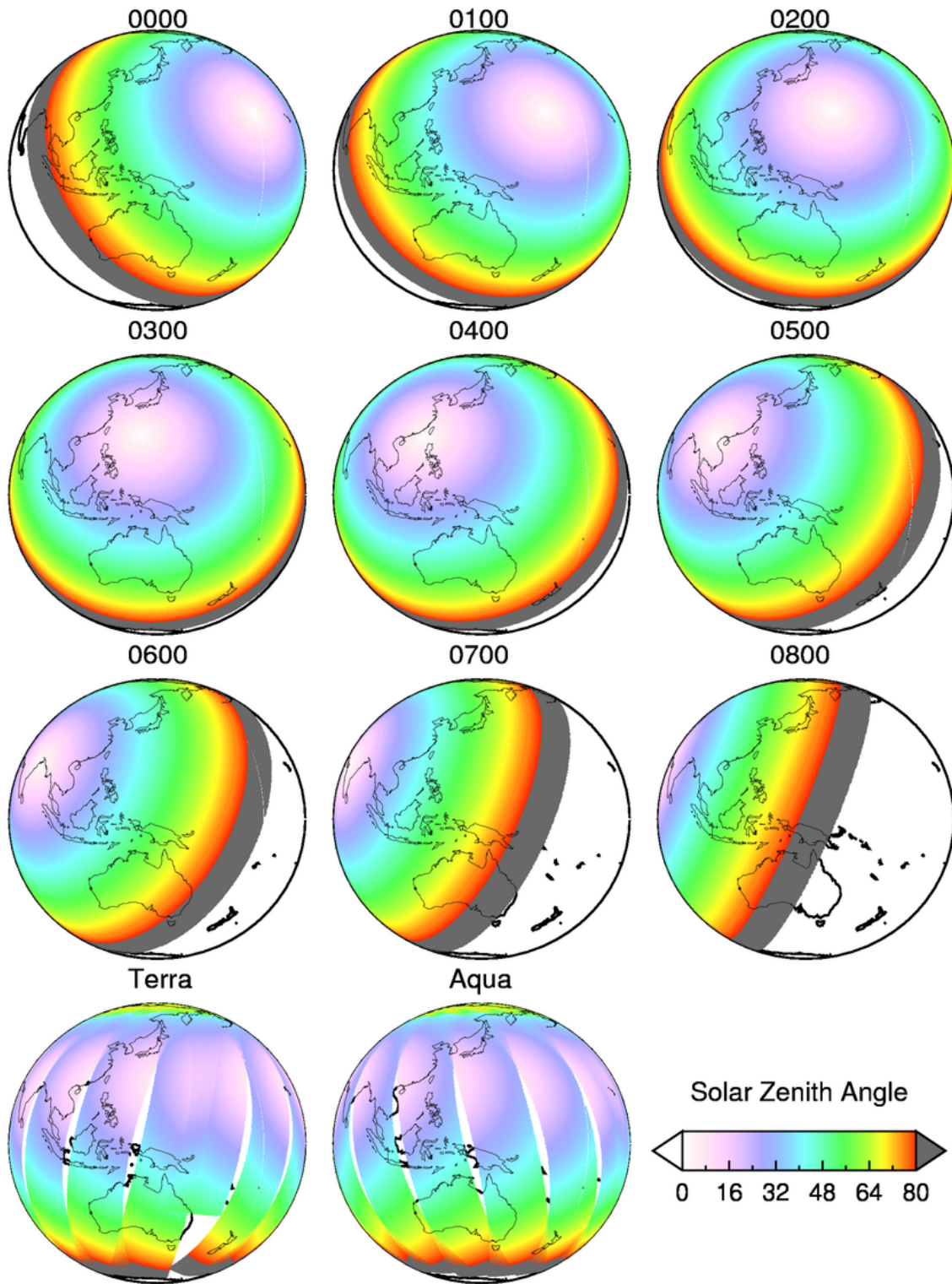
810

811

812 Figure 11. Mean solar zenith angle associated with each of the diurnal hours from the

813 AHI geometry and also for MODIS on Terra and Aqua for May 29, 2016.

814 There also appears to be another AOD retrieval artifact over the ocean associated with the
815 glint angle. Here AODs seem artificially high. Incorrect estimation of wind speed from
816 ancillary data or modeling of the rough ocean surface will introduce near-glint mask
817 inaccuracies in the AOD retrieval. With MODIS, such areas were relatively small and the
818 overall effect on global or regional AOD minimal. In the geosynchronous view, because
819 the glint mask is such a dominant feature, the near-glint artifacts appear much more
820 pronounced.

821

822 The good news seen in Figure 10 is that the retrieval over land does not appear to have
823 encountered any systematic artifacts. Blue and red shading is distributed spottedly across
824 the Asian, Indonesian and Australian land masses. Without validation we cannot say for
825 sure, but typically local factors determine aerosol diurnal trends, and thus, the spotty
826 blue/red shading could indicate that the retrieved AOD is representing the consequences
827 of these local diurnal forcing mechanisms. We have already seen in Figures 7 and 8 that
828 the AHI retrievals resolved the differing local diurnal patterns at three over land
829 AERONET stations within relative close proximity. In terms of the over land retrieval,
830 Figure 10 demonstrates that the DT algorithm applied to AHI will identify land regions
831 where the diurnal signal is more spatially cohesive. For example the east coast of India
832 and Bangladesh experience an increase in AOD in the late afternoon, while the overall
833 trend in northeast China is to decrease AOD in the afternoon, although there are local
834 contradictions to these regional patterns.

835

836 **4.3 AHI-derived AOD diurnal cycle over 5-degree squares**

837

838 The factors that drive a diurnal AOD signature tend to be local in character. These
839 include sources and sinks linked to time-of-day (rush hour traffic, agricultural burning,
840 afternoon convection/precipitation) or diurnally influenced mesoscale circulations and
841 transport (sea breeze or mountain slope regimes). Thus, individual stations as shown in
842 Figure 7 exhibit stronger diurnal signatures than does an ensemble average consisting of
843 stations distributed across the region (bottom right panel of Figure 7). The full disk plots
844 of Figure 10 suggest that there are regions of moderate extent that do experience a

845   cohesive diurnal AOD pattern. To further investigate the ability of the DT AHI to provide

846   insight into diurnal patterns of AOD during daylight hours we calculate the average AOD

847   in specific 5° latitude by 5° longitude boxes as a function of the hour of the day.

848

849   Figure 12 shows the diurnal AOD signatures of five of these 5° by 5° boxes. As suggested

850   by Figure 10, the AOD over northeastern China (Fig. 12, Box# 1) exhibits its highest

851   AOD during morning hours, 00 UTC to 03 UTC, corresponding to local times of 0800 to

852   1100, then experiences a slow decrease during the remainder of the day until sunset.

853   Average mean AOD at 550 nm in this area ranges from morning values of 0.65 to late

854   afternoon values of less than 0.40. Over Bangladesh (Fig. 12, Box #2) the glint mask

855   does not interrupt ocean retrievals until the last diurnal hour of the day. Ocean and land

856   retrievals exhibit very similar diurnal signatures in this area, slowly rising from morning

857   lows of 0.3-0.4 to late afternoon highs of 0.8-0.9, at least over land. Another area

858   containing both land and ocean retrievals is over northern Japan and adjacent Pacific

859   Ocean (Fig. 12, Box #3). This area is far enough north to not be hampered by the glint

860   mask at this time of year. The over ocean and over land diurnal patterns are similar with

861   morning to midday values of 0.30-0.35 gradually decreasing through the afternoon to

862   lows of 0.15 by sunset. This is a significant diurnal range of AOD over ocean.

863

864

865

866
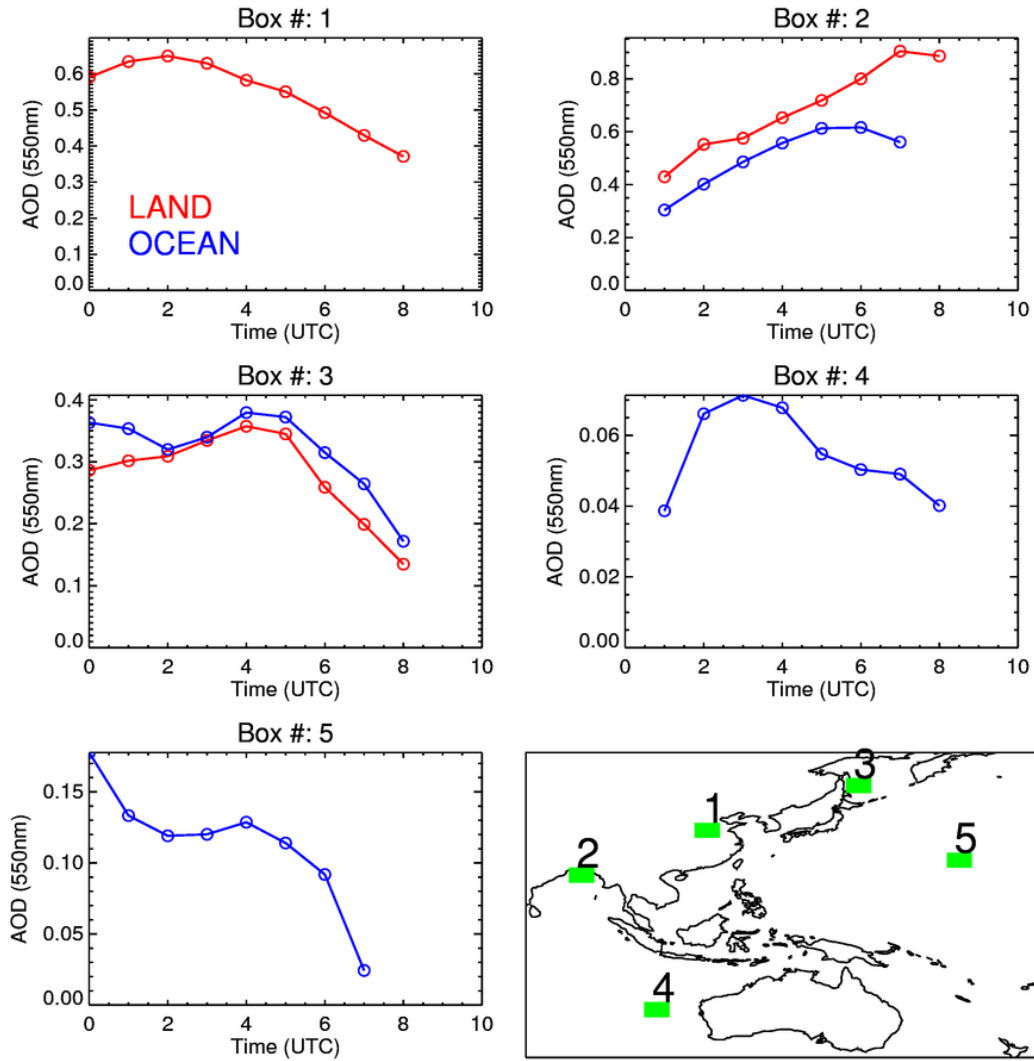
867   Figure 12. Spatially averaged mean AOD at 550 nm from the derived DT AHI product

868   for selected 5º by 5º latitude-longitude squares (boxes) in each hourly bin for the two-

869   month study period, producing AOD diurnal signatures for these selected areas. Red lines

870   depict over land retrievals. Blue lines depict over ocean retrievals. X-axes are in UTC

871   hours, for the reference, the local time in Beijing is +8 hours from UTC. Y-axes scale

872   vary from plot to plot. The green squares on global map indicate location of the specific

873   box.

874

875   Two areas over open ocean are shown in Figure 12, one in the Indian ocean west of

876   Australia (Fig. 12 Box #4) and the other in the Pacific (Fig. 12, Box #5). Note that the

877   scales on the y-axes of these two plots are different. At the Indian ocean area there

878   appears to be a diurnal signal, but the amplitude of that signal is only about 0.02, well

879   within the noise levels of both the retrieval itself and of the sampling and statistics of

880   calculating the diurnal pattern. Essentially there is no significant diurnal signal at this

881   location and the mean AOD is about 0.05±0.01. In contrast the Pacific example exhibits a

882   strong diurnal pattern, ranging almost an order of magnitude from 0.18 (~0.2) to 0.02. It

883   is in this area that the two ocean artifacts become apparent. During the early morning

884   hours this area resides just north of the sun glint mask where insufficient modeling of the

885   rough ocean surface creates an artifact in the retrieval, introducing a high bias. During

886   late afternoon hours, the solar zenith angle increases to beyond 70º and the low bias

887   artifact from the terminator affects the retrieval. It is only midday day when this Pacific

888   region escapes either artifact and then we see little diurnal signature and a mean AOD of

889   0.11 ± 0.015. Thus, the apparently strong diurnal signal here is in reality just the

890   combination of two different artifacts in the retrieval.

891

892   The examples in Figure 12 illustrate the variety of aerosol diurnal patterns over Asia with

893   polluted regions like northeastern China and Bangladesh showing diurnal amplitudes of

894   0.25 – 0.50 in AOD, but with oppositely signed slopes. The need to understand and

895   explain these different patterns across an area as large as Asia opens new research

896   questions as to what is the driving processes behind these AOD patterns, how will they

897   affect assimilation into global and regional models, and what are the air quality and

898   public health implications? While the processes creating diurnal aerosol patterns are

899   primarily local, the consequences of spatially cohesive patterns will have non-local

900   consequences, and aerosol products from geosynchronous observations, such as the AHI

901   DT product, are key to identifying and quantifying these spatially cohesive situations.

902   The patterns seen in Figure 12 may also suffer from the caveats imposed upon the

903   individual station analysis of Figure 7. The diurnal patterns may be artificial constructs of

904   observations made at different times on different days and not represent the true change

905   of aerosol loading over the span of day light hours. However, because of the greater

906   statistical sample offered by the larger spatial domain of the 5º x 5º box there is greater

907   confidence in the patterns of Figure 12 than those of Figure 7.

908   The examples in Figure 12 also illustrate that artifacts still exist in the retrieval over the

909   ocean, but that not all strong diurnal signatures over ocean are due to the artifacts, as

910   shown in Fig. 12d where the ocean pattern mimics the artifact-free land pattern. Being

911   aware of the possibility of artifacts and working towards mitigating those artifacts in the

912   future will be essential to properly making use of any new geosynchronous product.

913

914   **5.0 Discussion and conclusions**

915

916   The traditional Dark Target (DT) aerosol retrieval algorithm was adapted for the

917   Advanced Himawari Imager (AHI) and applied to AHI-measured spectral reflectances

918   produced for a limited data set in support of KORUS-AQ for the two-month period of

919   May-June 2016. The adaptation makes use of the spectral similarity between AHI and its

920   predecessor DT sensors (e.g. MODIS, VIIRS), but omits certain important pixel selection

921   procedures that require spectral bands unavailable from AHI. The lack of these specific

922   masks may permit additional cirrus and cloud contamination into the results of this two-

923   month preliminary demonstration, although large-scale comparisons of collocated AHI

924   and AERONET or AHI and MODIS retrievals do not reveal significant overall biases.

925   However, AHI retrievals may be benefitting from AERONET or MODIS cloud masking

926   in the collocations. Expanding the AHI retrieval into the winter months when snow/ice

927   will be encountered will then certainly show contamination from such surfaces, as the

928   current DT snow/ice mask requires the 1.24 μm channel that is missing from AHI. Before

929   wintertime retrievals are made with AHI, a new cloud/ice mask for this sensor must be

930   developed.

931

932   Collocations between AHI and AERONET demonstrate that AHI retrievals match

933   AOD_550 nm at AERONET stations as well as the MODIS DT aerosol product matches

934   AERONET in terms of correlation, RMSE, overall bias and percentage within expected

935   error. Additionally, because AHI can make aerosol retrievals multiple times per day,

936   there were approximately twice as many AHI-AERONET collocations as there were

937   from MODIS-AERONET. Geostationary aerosol retrievals will significantly increase the

938   sampling of retrieved AOD from current polar-orbiting sensors. Not only did the DT AHI

939 product match AERONET, statistically, in scatterplots, it also represented the diurnal

940 signal in AOD, as measured by AERONET at individual stations, and in the ensemble

941 median statistics. The three stations shown are representative of varying retrieval biases

942 and exhibit different diurnal signatures, even though they are in relatively close

943 proximity. The AHI DT algorithm was able to distinguish these diurnal differences,

944 although sample size was small and signal-to-noise impeded inference of the diurnal

945 signature.

946

947 Plotting the time series of the collocated data along the same axis shows that the AHI

948 AOD matches the temporal variability of the AERONET AOD hour-by-hour, even when

949 there is a strong bias in the magnitude. These time series plots are strong evidence that

950 the DT retrieval algorithm applied to geosynchronous sensors such as AHI will be able to

951 resolve short duration events such as individual plumes when the algorithm moves to

952 operational status.

953

954 Collocated AHI and MODIS retrievals demonstrate excellent agreement when applying

955 the DT algorithm to the two different sensors. Both AHI and MODIS produce similar

956 representations of the 2-month mean AOD across the AHI full disk region. However,

957 difference maps do show regional biases. Interestingly, AHI is overall biased low against

958 MODIS-Terra, but biased high against MODIS-Aqua, and thus falling within the offsets

959 already noted between the AODs of the two MODIS sensors (Levy et al., 2018). The one

960 place that AHI differs in the same way from both MODIS-Terra and MODIS-Aqua is in

961 its positive bias of 0.10 in the high aerosol loading regions of south, southeast and

962 northeast Asia. The fact that these biases are only seen in high aerosol loading suggests a

963 problem with the traditional DT aerosol models, not the surface parameterization. We

964 note that the over land aerosol models have never been tested for the unique geometry

965 that AHI has brought to the table.

966

967 When the algorithm is applied to the full disk image and hourly mean AOD plots are

968 made, we notice immediately an artifact in the diurnal signature that affects only the over

969 ocean retrieval. This artifact occurs at the day/night terminator and is associated with

970 extreme solar zenith angles, not view angles. Extreme solar zenith angles are much more

971 prevalent in geosynchronous images than in polar-orbiting ones, and thus our previous

972 experience with polar-orbiting sensors did not prepare us for this artifact. The most likely

973 explanation for the solar zenith artifact is the inability of the original radiative transfer

974 code to model spherical Earth. Earth's curvature when the sun is on the horizon will

975 introduce uncertainties into the radiative transfer calculation and result in inaccurate

976 aerosol retrievals. Until modifications can be made to the radiative transfer code, the

977 solution to mitigating this artifact will be to limit retrievals to lower solar zenith angles

978 over ocean (<70º). This is unfortunate because already the retrieval loses a goodly section

979 of the equatorial ocean because of the 40º glint mask when solar zenith angles are small.

980 Because we also saw retrieval artifacts along the edge of the glint mask, it is unlikely that

981 the 40º threshold can be relaxed. For now, the DT AHI retrieval over ocean should be

982 limited to a small range of solar zenith angles that will avoid both the glint and the

983 artifact at the terminator, and this will limit the diurnal range of AHI-retrieved AOD over

984 ocean.

985

986 In a preliminary analysis meant to show the scientific potential of the AHI DT product

987 we found a balance between the local nature of diurnal signatures and the need of a

988 substantial statistical sample by calculating the mean diurnal patterns of AOD in 5º

989 latitude by 5º longitude boxes. The result of this analysis revealed a variety of diurnal

990 patterns across Asia, as well as illustrating diurnal patterns of ocean areas affected and

991 not affected by glint and solar zenith angle artifacts. A more mature AHI DT product

992 will enable further exploration of these diurnal patterns and the consequences these

993 patterns hold for climate processes, assimilation systems and air quality.

994

995 To make progress towards a more mature algorithm beyond the preliminary version

996 analyzed here, we will need to continue the analysis and investigate the following points:

997

998 • What is the reason for the biases between AHI and both AERONET and MODIS?

999 • Are these biases linked to solar zenith angle, view angle or scattering angle?

1000   •   Are these biases linked to surface parameterization? Specifically change in
1001   surface ratios with viewing geometry.
1002   •   Do we mitigate artifacts by employing a more realistic spherical radiative transfer
1003   code?
1004   •   How do we mask for snow/ice without the 1.24 μm wavelength?
1005   •   Can we characterize cloud and cirrus contamination in the retrievals, and then
1006   mitigate those effects?
1007   •   How does the retrieved AOD spectral dependence and size parameter from AHI
1008   compare to those from MODIS?
1009   •   Can we surpass results obtained from the polar orbiting sensors by incorporating
1010   additional specific geosynchronous capabilities into the DT retrieval?
1011

1012 The short two-month demonstration described and illustrated here is a preliminary

1013 assessment of the ability to bring the well-vetted DT aerosol retrieval to a

1014 geosynchronous satellite sensor. The results show that porting the algorithm is possible,

1015 that it can produce AOD that matches AERONET to the same degree as the MODIS

1016 product, and that it can distinguish local diurnal signatures at AERONET stations over

1017 land. The view from geosynchronous sensors will provide new insight into Earth's

1018 aerosol system, especially if that view is steeped in and compatible with the 20-year

1019 record of the DT polar-orbiting experience. This study puts us on the road to achieving

1020 this new perspective.

1021

1022 **6. Acknowledgement**

1023

1024 This work was supported by the NASA ROSES program NNH17ZDA001N: Making

1025 Earth System Data Records for Use in Research Environments and NASA's EOS

1026 program managed by Hal Maring. We thank Space Science and Engineering Center

1027 (SSEC), University of Wisconsin-Madison for providing Himawari-8 data. We thank

1028 MCST for their efforts to maintain and improve the radiometric quality of MODIS data,

1029 and LAADS/MODAPS for the continued processing of the MODIS products. The

1030 AERONET team (GSFC and site PIs) are thanked for the creation and continued

1031   stewardship of the sun photometer data record; which is available from

1032   http://aeronet.gsfc.nasa.gov.

1033

1034   **7. References**

1035

1036   Ahmad Z. and Fraser R.: An iterative radiative transfer code for ocean-atmosphere

1037   systems, J. Atmos. Sci.,32, 656-665, doi:10.1175/1520-0469(1982)039, 1982.

1038   Boucher, O., et al.: Clouds and aerosols. In: Climate Change 2013: The Physical Science

1039   Basis. Contribution of Working Group I to the Fifth Assessment Report of the

1040   Intergovernmental Panel on Climate Change [Stocker, T. F., D. Qin, G.-K. Plattner,

1041   M. Tignor, S. K. Allen, J. Boschung, A. Nauels, Y. Xia, V. Bex, and P. M. Midgley

1042   (eds.)]. Cambridge University Press, Cambridge, United Kingdom and New York,

1043   NY, USA, 2013.

1044   Diner, D. J., Beckert, J. C., Reilly, T. H., Bruegge, C. J., Conel, J. E., Kahn, R. A.,

1045   Martonchik, J. V., Ackerman, T. P., Davies, R., Gerstl, S. A. W., Gordon, H. R.,

1046   Muller, J.-P., Myneni, R. B., Sellers, P. J., Pinty, B., and Verstraete, M. M.: Multi-

1047   angle Imaging SpectroRadiometer (MISR) instrument description and experiment

1048   overview, IEEE T. Geosci. Remote, 36, 1072–1087, doi:10.1109/36.700992, 1998.

1049   Diner, D. J., Abdou, W. A., Ackerman, T. P., Crean, K., Gordon, H. R., Kahn, R. A.,

1050   Martonchik, J. V., McMuldroch, S., Paradise, S. R., Pinty, B., Verstraete, M. M.,

1051   Wang, M., and West, R. A.: Multi-Angle Imaging SpectroRadiometer Level 2 Aerosol

1052   Retrieval Algorithm Theoretical Basis, Revision G, JPL D-11400, Jet Propulsion

1053   Laboratory, California Institute of Technology, Pasadena, USA, 2008.

1054   Eck, T. F., Holben, B.N., Reid, J.S., Dubovik, O., Smirnov, A., O'Neill, N.T., Slutsker, I.,

1055   and Kinne, S., Wavelength dependence of the optical depth of biomass burning, urban,

1056   and desert dust aerosols, J. Geophys. Res. – Atmos., 104, 31333–31349,

1057   doi:10.1029/1999JD900923, 1999.

1058   Frey, R. A., Ackerman, S. A., Liu, Y., Strabala, K. I., Zhang, H., Key, J. R., & Wang, X.:

1059   Cloud detection with MODIS. Part I: Improvements in the MODIS cloud mask for

1060   collection 5., J. Atmos. Ocean. Tech., 25, 1057-1072, 2008.

1061 Gupta, P., Levy, R.C., Mattoo, S., Remer, L.A., and Munchak, L.A.: A surface
1062   reflectance scheme for retrieving aerosol optical depth over urban surfaces in MODIS
1063   Dark Target retrieval algorithm, Atmos Meas Tech, 9, 3293–3308, doi:10.5194/amt-9-
1064   3293-2016, 2016.

1065 Gupta, P., Remer, L. A., Levy, R. C., and Mattoo, S.: Validation of MODIS 3 km land
1066   aerosol optical depth from NASA's EOS Terra and Aqua missions, Atmos. Meas.
1067   Tech., 11, 3145-3159, https://doi.org/10.5194/amt-11-3145-2018, 2018.

1068 Hsu, N.C., Tsay, S.C., King, M.D. and Herman, J.R.: Aerosol properties over bright-
1069   reflecting source regions. IEEE Trans. Geosci. Rem. Sens. 42. 557-569. doi:
1070   10.1109/TGRS.2004.824067, 2004.

1071 Hsu, N.C., Jeong, M.-J., Bettenhausen, C., Sayer, A.M., Hansell, R., Seftor, C.S., Huang,
1072   J. and Tsay, S.-C.: Enhanced Deep Blue aerosol retrieval algorithm: The second
1073   generation. J. Geophys. Res. – Atmos. 118, 9296-9315, doi:10.1002/jgrd.50712, 2013.

1074 Ichoku, C., Chu, D.A., Mattoo, S., Kaufman, Y.J., Remer, L.A., Tanre, D., Slutsker, I.,
1075   and Holben, B.N., A spatio-temporal approach for global validation and analysis of
1076   MODIS aerosol products, Geophys Res Lett, 29, doi:10.1029/2001GL013206, 2002.

1077 Jickells, T.D., An, Z.S., Andersen, K.K. et al., Global iron connections between desert
1078   dust, ocean biogeochemistry, and climate. Science, 308, 67-71, doi:
1079   10.1126/science.1105959, 2005

1080 Kahn, R. A., Gaitley, B. J., Garay, M. J., Diner, D. J., Eck, T., Smirnov, A., and Holben,
1081   B. N.: Multiangle Imaging SpectroRadiometer global aerosol product assessment by
1082   comparison with the Aerosol Robotic Network, J. Geophys. Res., 115, D23209,
1083   doi:10.1029/2010JD014601, 2010.

1084 Kahn, R. A., and Gaitley, B.J.: An analysis of global aerosol type as retrieved by MISR.
1085   J. Geophys. Res. Atmos., 120, 4248–4281, doi:10.1002/2015JD02332, 2015.

1086 Kalashnikova, O.V., and Kahn, R.: Ability of multiangle remote sensing observations to
1087   identify and distinguish mineral dust types: Part 2. Sensitivity over dark water, J.
1088   Geophys. Res. Atmos., 111, D11207, doi:10.1029/2005JD00675, 2006.

1089 Kalluri, S., Alcala, C., Carr, J., Griffith, P., Lebair, W., Lindsey, D., Race, R., Wu, X.,
1090   and Zierk, S.: From photons to pixels: Processing data from the Advance Baseline
1091   Imager, Remote Sensing, 10, 10.3390/rs10020177, 2018.

1092   Kaufman, Y. J., Koren, I., Remer, L. A., Tanré, D., Ginoux, P. and Fan, S.: Dust transport and

1093   deposition observed from the Terra-MODIS spacecraft over the Atlantic Ocean, J Geophys.

1094   Res., 110, D10S12, doi:10.1029/2003JD004436,2005

1095   Koren, I., Kaufman, Y.J., Rosenfeld, D., Remer, L.A. and Rudich, Y.: Aerosol

1096   invigoration and restructuring of Atlantic convective clouds, Geophys. Res. Lett., 32,

1097   LI4828, doi: 10.1029/2005GL023187, 2005.

1098   Levy, R. C., Remer, L.A. and Dubovik, O.: Global aerosol optical properties and

1099   application to Moderate Resolution Imaging Spectroradiometer aerosol retrieval over

1100   land, J Geophys Res-Atmos, 112, D13210, doi:10.1029/2006JD007815, 2007a.

1101   Levy, R. C., Remer, L.A., Mattoo, S., Vermote, E.F. and Kaufman, Y.J.: Second-

1102   generation operational algorithm: Retrieval of aerosol properties over land from

1103   inversion of Moderate Resolution Imaging Spectroradiometer spectral reflectance, J.

1104   Geophys. Res.-Atmos., 112, D13211, doi:10.1029/2006JD007811, 2007b.

1105   Levy, R.C., S. Mattoo, L.A. Munchak, L.A. Remer, A. Sayer, N.C. Hsu. The Collection 6

1106   MODIS aerosol products over land and ocean. Atmos. Meas. Tech., 6, 2989-3034,

1107   2013.

1108   Levy, R.C., Munchak, L.A., Mattoo, S., Patadia,F., Remer, L.A. and Holz, R.E. :

1109   Towards a long-term global aerosol optical depth record: applying a consistent aerosol

1110   retrieval algorithm to MODIS and VIIRS-observed reflectance. Atmos. Meas. Tech.,

1111   8, 4083-4110, https://doi.org/10.5194/amt-8-4083-2015, 2015.

1112   Li, R.-R., Kaufman, Y.J., Gao, B.-C. and Davis, C.O.: Remote sensing of suspended

1113   sediments and shallow coastal waters. IEEE Trans. Geosci. Remote Sens., 41, 559–

1114   566, 2003.

1115   Lim, H., Choi, M., Kim, M., Kim, J., and Chan, P. W.: Retrieval and validation of

1116   aerosol optical properties using Japanese next generation meteorological satellite,

1117   Himawari-8. Korean Journal of Remote Sensing, 32, 681-691, 2016.

1118   Lim, H., Choi, M., Kim, M., Kim, J., Go, S., and Lee, S.: Intercomparing the Aerosol

1119   Optical Depth Using the Geostationary Satellite Sensors (AHI, GOCI and MI) from

1120   Yonsei AErosol Retrieval (YAER) Algorithm. J. Korean Earth Science Society, 39,

1121   119-130, 2018.

1122   Lim, H., Choi, M., Kim, J., Kasai, Y., and Chan, P. W.: AHI/Himawari-8 Yonsei Aerosol

1123   Retrieval (YAER): Algorithm, Validation and Merged Products. Remote

1124   Sensing, 10(5), 699, 2018.

1125   Lim, S.S., Vos, T., Flaxman, A.D., et al.: A comparative risk assessment of burden of

1126   disease and injury attributable to 67 risk factors and risk factor clusters in 21 regions,

1127   1990-2010: a systematic analysis for the Global Burden of Disease Study 2010.

1128   Lancet, 380, 2224-2260, 2012.

1129   Lin, J. C., Matsui, T., Pielke Sr., R.A., and Kummerow , C.: Effects of biomass-burning-

1130   derived aerosols on precipitation and clouds in the Amazon Basin: a satellite-based

1131   empirical study, J. Geophys. Res., 111, D19204, doi:10.1029/2005JD006884, 2006.

1132   Lyapustin, A., Wang,Y., Laszlo, I., Kahn, R., Korkin, S., Remer, L., Levy, R. and Reid,

1133   J.S.: Multiangle implementation of atmospheric correction (MAIAC): 2. Aerosol

1134   algorithm. J. Geophys. Res. 116, D03211, doi:10.1029/2010JD014986, 2011.

1135   Martins, J. V., Tanré, D., Remer, L, Kaufman, Y., Mattoo, S. and Levy, R.: MODIS

1136   Cloud screening for remote sensing of aerosols over oceans using spatial variability,

1137   Geophys Res Lett, 29, 32139, doi:10.1029/2001GL013252, 2002.

1138   Martonchik, J. V., Diner, D. J., Kahn, R., Ackerman, T. P., Verstraete, M. M., Pinty, B.,

1139   and Gordon, H. R., 1998, Techniques for the retrieval of aerosol properties over land

1140   and ocean using multiangle imaging, IEEE Transactions on Geoscience and Remote

1141   Sensing, 36(4), 1212–1227.

1142   Munchak, L. A., Levy, R. C. Mattoo, S., Remer, L.A., Holben, B.N., Schafer, J.S.,

1143   Hostetler, C.A., and Ferrare, R.A.: MODIS 3 km aerosol product: applications over

1144   land in an urban/suburban region, Atmos Meas Tech, 6, 1747–1759, doi:10.5194/amt-

1145   6-1747-2013, 2013.

1146   Patadia, F., Gupta, P., and Christopher, S. A.: First observational estimates of global clear

1147   sky shortwave aerosol direct radiative effect over land, Geophys. Res. Lett., 35,

1148   L04810, https://doi.org/10.1029/2007GL032314, 2008.

1149   Petrenko, M., Ichoku, C., and Leptoukh, G.: Multi-sensor Aerosol Products Sampling

1150   System (MAPSS), Atmos Meas Tech, 5, 913–926, doi:10.5194/amt-5-913-2012, 2012.

1151 Prados, A. I., Kondragunta, S., Ciren, P. and Knapp, K.R.: GOES Aerosol/Smoke

1152   Product (GASP) over North America: Comparisons to AERONET and MODIS

1153   observations, J. Geophys. Res., 112, D15201, doi: 10.1029/2006JD007968, 2007.

1154 Quaas, J., Ming, Y., Menon, S., Takemura, T., Wang, M., Penner, J. E.,and Sayer, A. M.:

1155   Aerosol indirect effects–general circulation model intercomparison and evaluation

1156   with satellite data. Atmos. Chem. Phys., 9, 8697-8717, 2009.

1157 Remer, L.A., Kaufman, Y.J., Tanré, D., Mattoo, S., Chu, D.A., Martins, J.V., Li, R.,

1158   Ichoku, C., Levy, R.C., Kleidman, R.G., Eck, T.F., Vermote, E. and Holben,

1159   B.N.: The MODIS Aerosol Algorithm, Products, and Validation. J. Atmos.

1160   Sci., 62, 947–973, 2005.

1161 Remer, L. A., Mattoo, S., Levy, R.C., Heidinger, A., Pierce, R.B., and Chin, M.:

1162   Retrieving aerosol in a cloudy environment: aerosol product availability as a function

1163   of spatial resolution, Atmos Meas Tech, 5, 1823–1840, doi:10.5194/amt-5-1823-2012,

1164   2012.

1165 Rosenfeld, D., Sherwood, S., Wood, R. and Donner, L.: Climate effects of aerosol-cloud

1166   interactions. Science, 343, 379-380, DOI: 10.1126/science.1247490, 2014a.

1167 Rosenfeld, D., Andreae, A. and Asmi, A.: Global observations of aerosol-cloud-

1168   precipitation-climate interactions. Rev. Geophys. 52, 750–808,

1169   doi:10.1002/2013RG000441, 2014b.

1170 Sekiyama, T. T., Yumimoto, K., Tanaka, T. Y., Nagao, T., Kikuchi, M., & Murakami, H.

1171   :Data assimilation of Himawari-8 aerosol observations: Asian dust forecast in June

1172   2015. Sola, 12, 86-90, 2016.

1173 Seinfeld, John H., et al.: Improving our fundamental understanding of the role of

1174   aerosol− cloud interactions in the climate system. Proc. Nat. Acad. Sci., 113, 5781-

1175   5790, 2016.

1176 Shi, S., Cheng, T., Gu, X., Letu, H., Guo, H., Chen, H., and Wu, Y.: Synergistic Retrieval

1177   of Multi-temporal Aerosol Optical Depth over North China Plain Using Geostationary

1178   Satellite Data of Himawari-8. Journal of Geophysical Research: Atmospheres, 123,

1179   5525–5537. https://doi.org/10.1029/2017JD027963.

1180 Tanré, D., Herman, M. and Kaufman, Y.: Information on the aerosol size distribution

1181   contained in the solar reflected spectral radiances, J. Geophys. Res., 101,

1182   19,043−19,060, 1996.

1183 Tanré, D., Kaufman, Y.J., Herman, M., and Mattoo, S.: Remote sensing of aerosol

1184   properties over oceans using the MODIS/EOS spectral radiances, J. Geophys. Res.,

1185   102, 16,971−16,988, 1997.

1186 Tanré, D., Bréon, F. M., Deuzé, J. L., Dubovik, O., Ducos, F., François, P., Goloub, P.,

1187   Herman, M., Lifermann, A., and Waquet, F. : Remote sensing of aerosols by using

1188   polarized, directional and spectral measurements within the A-Train: the PARASOL

1189   mission, Atmos. Meas. Tech., 4, 1383-1395, https://doi.org/10.5194/amt-4-1383-2011,

1190   2011.

1191 Torres, O., Tanskanen, A., Veihelman, B. , Ahn, C. , Braak, R., Bhartia, P. K. , Veefkind,

1192   P. and Levelt, P. : Aerosols and surface UV products from OMI observations: An

1193   overview, J. Geophys. Res., 112, D24S47, doi: 10.1029/2007JD008809, 2007.

1194 Torres, O., Ahn, C., and Chen, Z.: Improvements to the OMI near-UV aerosol algorithm

1195   using A-train CALIOP and AIRS observations. Atmos. Meas. Tech., 6, 3257-3270,

1196   doi:10.5194/amt-6-3257-2013, 2013.

1197 Uesawa, D.: Aerosol Optical Depth product derived from Himawari-8 data for Asian dust

1198   monitoring, Meteorological Satellite Center Technical Note, No.61, 2016..

1199 Wang, J. and Christopher, S. A.: Intercomparison between satellite-derived aerosol

1200   optical thickness and PM2. 5 mass: Implications for air quality studies. Geophys, Res.

1201   Lett., 30, 2095, doi:10.1029/2003GL018174, 2003.

1202   Yan, X., Li, Z., Luo, N., Shi, W., Zhao, W., Yang, X., and Jin, J.: A minimum albedo

1203   aerosol retrieval method for the new-generation geostationary meteorological satellite

1204   Himawari-8, Atmos. Res., 207, 14-27, 2018.

1205 Yang, F., Wang, Y., Tao, J., Wang, Z., Fan, M., de Leeuw, G., and Chen, L.: Preliminary

1206   Investigation of a New AHI Aerosol Optical Depth (AOD) Retrieval Algorithm and

1207   Evaluation with Multiple Source AOD Measurements in China, Rem. Sens., 10, 748,

1208   2018.

1209 Yoshida, M., Kikuchi, M., Nagao, T. M., Murakami, H., Nomaki, T., and Higurashi, A.:.

1210   Common retrieval of aerosol properties for imaging satellite sensors, J. Meteorol. Soc.

1211   Japan. Ser. II, 2018.

1212 Yu, F. and Wu, X.: Radiometric Inter-Calibration between Himawari-8 AHI and S-NPP

1213   VIIRS for the Solar Reflective Bands, Rem. Sens., 8, 165, 2016.

1214   Yu, Hongbin, Remer, L.A., Chin, Mian, Bian, Huisheng, Tan, Qian, Yuan, Tianle and

1215   Zhang, Yan, Aerosols from overseas rival domestic emissions over North America,

1216   Science 337, 566-569, doi: 10.1126/science.1217576, 2012.

1217   Yu, Hongbin, Remer, L.A., Kahn, R.A., Chin, Mian and Zhang, Yan (2013). Satellite

1218   perspective of aerosol intercontinental transport: From qualitative tracking to

1219   quantitative characterization, Atmos. Res. 124, 73-100, doi:

1220   10.1016/j.atmosres.2012.12.013, 2013.

1221   Yu, H., Chin, M., Yuan, T.L., Bian, H., Remer, L.A., Prospero, J.M., Omar, A., Winker,

1222   D., Yang,Y.K., Zhang, Y., Zhang, Z. and Zhao, C.: The fertilizing role of African dust

1223   in the Amazon rainforest: A first multiyear assessment based on data from Cloud-

1224   Aerosol Lidar and Infrared Pathfinder Satellite Observations, Geophys. Res. Lett., 42,

1225   1984-1991, doi: 10.1002/2015GL063040, 2015.

1226   Yumimoto, K., Nagao, T. M., Kikuchi, M., Sekiyama, T. T., Murakami, H., Tanaka, T.

1227   Y., and Arai, K.: Aerosol data assimilation using data from Himawari-8, a next-

1228   generation geostationary meteorological satellite. Geophys. Res.Lett., 43, 5886-5894,

1229   2016.

1230   Zhang, J., Christopher, S.A., Remer, L.A. and YKaufman, Y.J.: Shortwave aerosol

1231   radiative forcing over cloud-free oceans from Terra: 2. Seasonal and global

1232   distributions, J. Geophys. Res., 110, D10S24, doi:10.1029/2004JD005009, 2005.

1233   Zhang, W., Xu, H., and Zheng, F.: Aerosol Optical Depth Retrieval over East Asia Using

1234   Himawari-8/AHI Data, Rem. Sens., 10, 137, 2018.

1235

1236